Texture development and elastic stresses in magnesiowűstite at high pressure

Caterina E. Tommaseo*[1], Jim Devine[2], Sébastien Merkel[1], Sergio Speziale[1] and Hans-Rudolf Wenk[1]

[1]Department Earth and Planetary Science, University of California, Berkeley, CA 94720, USA
[2]University of Chicago, Geophysical Science, Chicago, IL 60637, USA

Abstract

Cubic magnesiowűstite has been deformed in a diamond anvil cell at room temperature. We present results for $(Mg_{0.4}Fe_{0.6})O$, $(Mg_{0.25}Fe_{0.75})O$ and $(Mg_{0.1}Fe_{0.9})O$ up to 37 GPa, 16 GPa and 18 GPa, respectively. The diffraction images, obtained with the radial diffraction technique, are analyzed using both single peak intensities and a Rietveld method. For all samples, we observe a [100] fiber texture but the texture strength decreases with increasing iron content. This texture pattern is consistent with {110}<1-10> slip. The images were also analyzed for stress, elastic strains and elastic anisotropy. In general, the stress measured in magnesiowűstite samples is lower than previously measured on MgO. The elastic anisotropy deduced from the X-ray measurements shows a broad agreement with models based on measurements with other techniques.

Keywords: (Mg,Fe)O, texture, DAC, synchrotron X-rays, deformation mechanisms, magnesiowűstite, elasticity

*Caterina E. Tommaseo
497 McCone Hall
Phone (510) 642-7431
Fax (510) 643-9980
E-mail: tommaseo@eps.berkeley.edu

1. Introduction

Magnesiowűstite ((Mg,Fe)O) is a major component of the lower mantle and its deformation behavior is important for understanding the rheology of the deep earth. The amount of Fe present in (Mg,Fe)O in the lower mantle has been estimated to be 10-45 mol% FeO, based on high P-T element partitioning experiments (e.g. Mao et al., 1997; Andrault, 2001 and references therein). Both wuestite, which has a non-stoichiometric formula $Fe_{1-x}O$ (e.g. McCammon, 1993), and periclase (MgO) have a NaCl (B1) structure at ambient conditions. Intermediate and iron-rich compositions of magnesiowűstite show a phase transition to a rhombohedral phase at high pressure (Yagi et al., 1985, Richet et al., 1989, Kondo et al., 2004, Lin et al., 2003). There is also a pressure-induced electronic spin transitions of iron in (Mg,Fe)O at high pressure (Sherman 1988, Sherman 1991, Sherman and Jansen 1995, Cohen et al 1997, Badro et al 2003, Lin et al 2005, Speziale et al 2005), and a possible dissociation of intermediate compositions into magnesium-rich and iron-rich components (Dubrovinsky et al., 2000; 2001; 2005). Magnesiowűstite is of central importance for geodynamics due to two unique properties. Firstly, its creep strength is likely to be considerably smaller than that of $(Mg,Fe)SiO_3$ perovskite (Yamazaki and Karato, 2001) and recent simulations suggest that perovskite will control the strength of the lower mantle while (Mg,Fe)O may accommodate most of the strain (Madi et al 2005). Secondly, despite its cubic crystal structure, (Mg,Fe)O is likely to have large elastic anisotropy: according to first principles calculations, elastic anisotropy in (Mg,Fe)O is similar to that of orthorhombic $(Mg,Fe)SiO_3$ perovskite at lower mantle conditions (Karki et al., 1997; Wentzcovitch et al., 1998). Consequently,

magnesiowűstite may contribute significantly to the development of seismic anisotropy (e.g. Karato, 1998 a,b).

Several studies have focused on texture development in periclase and magnesiowűstite. Merkel et al (2002) deformed MgO at room temperature and high pressure. Yamazaki and Karato (2002), Stretton et al. (2001) and Heidelbach et al (2003) deformed magnesiowűstite at moderate pressure and high temperature in torsion as well as axial compression. The results indicate that at low temperature {110}<1-10> is the only significantly active slip system, whereas at higher temperature {100} and {111} slips become equally active. In this report we investigate texture development in magnesiowűstite with compositions $(Mg_{0.4}Fe_{0.6})O$, $(Mg_{0.25}Fe_{0.75})O$ and $(Mg_{0.1}Fe_{0.9})O$ in axial compression at high pressure and room temperature, measured in situ by synchrotron X-ray diffraction and a diamond anvil cell (DAC), with the goal to study the influence of iron content on texture development and elastic properties.

2. Experimental Details

The starting materials were synthetic polycrystalline $(Mg_{0.4}Fe_{0.6})O$, $(Mg_{0.25}Fe_{0.75})O$ and $(Mg_{0.1}Fe_{0.9})O$ that belong to the collection of magnesiowűstites synthesized and investigated by Bonczar and Graham (1982). They were prepared by reacting finely ground and well mixed powders of oxides and iron in the appropriate proportions. To induce reaction, the palletized mixtures were sintered at 1000°C for several hours in iron crucibles within an evacuated silica tube. Samples were then ground

and the conversion to the B1 phase checked by X-ray diffraction. The chemical composition of the samples was determined using electron microprobe and wet chemical analyses. Before the present experiments, each sample was further ground in an alumina mortar and loaded as a powder in the DAC. The grain size of the starting material, estimated in a stereomicroscope (Stemi SV11) with a zoom range 11:1 with a built in scale, was in the submicron range.

We performed X-ray diffraction experiments in at the 16-IDB beamline of HPCAT at APS (Advanced Photon Source, Argonne National Laboratory) and at beamline 12.2.2. at ALS (Advanced Light Source, Lawrence Berkeley National Laboratory). For the experiments at HPCAT a monochromatic X-ray beam (λ=0.42275 Å), approximately 15-17 μm in diameter, was focused on the sample either through a beryllium gasket for $(Mg_{0.25}Fe_{0.75})O$ or amorphous boron and epoxy gasket for $(Mg_{0.4}Fe_{0.6})O$. Exposure time was 30 seconds for $(Mg_{0.25}Fe_{0.75})O$ and 1 second for $(Mg_{0.4}Fe_{0.6})O$. $(Mg_{0.1}Fe_{0.9})O$ samples were studied at beamline 12.2.2 at ALS using monochromatic X-ray beam (λ=0.4133 Å for the first run and λ=0.49593 Å for the second run). In this case, the 70 μm diameter beam was focused on the sample through a composite gasket made of an amorphous boron/epoxy disk confined within a kapton supporting ring (Merkel and Yagi, 2005a) with an exposure time of 240 seconds per image. Simple geometrical calculations indicate that for a beam of 15 μm and 70 μm diameter, the irradiated volume is on the order of 2.5 10^4 and 10^5 μm^3, respectively. Therefore, each diffraction image includes a contribution from thousands of grains and is appropriate for texture refinement.

In all experiments X-ray diffraction was measured in radial geometry with the DAC compression axis perpendicular to the incident beam. Diffraction images were recorded with a MAR345 image-plate system (3450x3450 pixels). On those images, the intensity variations along Debye rings are indicative of preferred orientation while variations in diffraction angles are related to stress and elasticity (**Figure 1a and b**). For the measurements performed at the APS the detector to sample distance, calibrated using a Si standard, was 36.12 cm, thus optimizing the range of diffraction rings recorded for the opening cone of a standard symmetric piston-cylinder DAC to $2\Theta max=18°$. In the experiments performed at beamline 12.2.2 at ALS, the sample to detector distance, calibrated using a LaB_6 standard, was 29.69 cm, thus optimizing the range of diffractions recorded for the opening cone of a large-opening Mao-Bell type DAC to $2\Theta max=26°$. In all cases, hydrostatic pressures were estimated from the lattice parameter of a gold standard, using the equation of state of gold (Anderson et al., 1989, Duffy et al., 1999). The uncertainty of the estimated pressures is ±3 GPa in average due to uncertainties in the equations of state of gold and non-hydrostatic stress conditions.

3. Data analysis

3.1 Rietveld analysis with MAUD

The X-ray diffraction images were analyzed with the Rietveld method using the software MAUD (Lutterotti et al., 1999, Lonardelli et al. 2005). This software refines

instrumental, structural, microstructural parameters and texture from continuous diffraction spectra. Spectra were obtained by integrating the images over 5° azimuthal angular slices resulting in 72 spectra per image. In some of the experiments a few spectra had to be removed due to a saturation of the image because of a few large grains. **Figure 2a and 2b** show representative spectra at different angles relative to the compression direction for $(Mg_{0.4}Fe_{0.6})O$ and $(Mg_{0.1}Fe_{0.9})O$ at 13 GPa.

For $(Mg_{0.4}Fe_{0.6})O$ and $(Mg_{0.25}Fe_{0.75})O$ we applied the Rietveld refinement method to all the azimuthal diffraction profiles with d-spacings ranging from 1.4 Å to 2.78 Å which included 111, 200, and 220 (**Figure 2a**). Diffraction profiles of $(Mg_{0.1}Fe_{0.9})O$ were refined over a d-spacing range from 0.92 Å to 2.78 Å (which includes six diffraction lines, 400, 222, 311, 220, 200, 111) (**Figure 2b**). Instrument parameters (detector distance, beam center, peak profile, and detector tilt) were refined on the calibrant patterns. For each image, we then refined four background parameters per orientation, crystallographic parameters, stress, and texture with a composite sample of (Mg,Fe)O and gold. Stress was assumed to be triaxial with $2\sigma_{11}=2\sigma_{22}=-\sigma_{33}$ (axial symmetry) and refined using a simple isotropic model based on Young's modulus and Poisson ratio.

In absence of experimental or theoretical data regarding the single-crystal elasticity of magnesiowűstite at high pressure we estimated the aggregate bulk and shear moduli of our sample using third order Eulerian strain equations (Davies, 1974) based on the ambient pressure bulk and shear moduli of Jacobsen et al. (2002) and the pressure derivatives of Bonczar and Graham (1982). Once a satisfying fit between the calculated and measured *d*-spacings was achieved, we applied the texture model EWIMV that relies

on the discrete tomographic method WIMV (Matthies and Vinel, 1982) to deduce the ODF (orientation distribution function) of the sample. The main difference between EWIMV and WIMV is that in EWIMV the ODF cell path for each data point is computed explicitly for the true measurement angles, no longer requiring a regular grid coverage and interpolation. In this process, we chose a resolution of 10° and a projection tube radius of 20°. First, no sample symmetry was imposed. Under this approximation, we were able to obtain qualitatively reasonable pole figures from a single image (e.g. Ischia et al. 2005) indicating overall axial symmetry with some deviations that can be attributed to the minimal pole figure coverage. **Figure 3a** presents the 100 pole figure obtained in such refinement for $(Mg_{0.4}Fe_{0.6})O$ at 13 GPa. In a second cycle of refinements, cylindrical symmetry was imposed and **Figure 3b** presents the symmetrical 100 pole figure obtained for the same conditions as **Figure 3a**. After confirming axial symmetry we assumed it for all results presented in this paper.

At the end of the Rietveld refinement in MAUD the ODFs were exported and further smoothed in BEARTEX (Wenk et al., 1998) with a 11° Gauss filter to reduce stochastic effects. From this smoothed ODF we calculated inverse pole figures that represent the probability of finding crystal directions parallel to the compression direction. Densities are expressed in multiples of a random distribution (m.r.d.). For axially symmetric texture, inverse pole figures provide a complete texture description. The texture is also represented by some numerical parameters such as minimum and maximum of the ODF and the texture index *F*2 (Bunge, 1982). The texture index is the integral over squared ODF values and thus it is a measure for the texture strength. Since all textures display a main concentration near 001 we also calculated how much grains

with the compression direction parallel to 001 contribute to the overall texture. This was done by calculating the orientation volume of a sphere centered at Euler angles α=0°, β=0°, γ=0° (Matthies convention) with a radius of 20° (program COMP in BEARTEX).

3.2 *Texture analysis with the single peak method*

One of the major difficulties encountered in the refinement of the X-ray diffraction data of magnesiowűstite is the presence of a large elastic strain anisotropy for different crystallographic directions. This reflects a strong directional dispersion of the Young's modulus *E(hkl)*. Based on data at ambient conditions (Jackson and Khanna, 1990; Sinogeikin and Bass, 2000; Jacobsen et al., 2002), the variation of Young's modulus between [100] and [111] ranges between 6% and 20% in the range of compositions investigated in this study. Because of this, texture analysis with the Rietveld method that uses an isotropic stress model was limited and we also applied a different approach based on single peak fit to extract texture and stress information.

In this second approach, we analyzed the variations in the position of the diffraction peaks and their intensity with the azimuthal angle δ by integrating intensities in 5° slices with the software FIT2D (Hammersley, 1998). For each image, this produces 72 segments for δ between 0° and 360°. The patterns were then fitted individually assuming Gaussian peak profiles and a linear local background. The pole distance χ, which corresponds to the angle between the diffracting plane normal and the load axis, was calculated from:

$$\cos\chi = \cos\theta\cos\delta, \qquad (1)$$

where θ is the diffraction angle (**see Figure 3 in Merkel et al., 2002**).

Using this alternative approach each peak was fitted individually, and the diffraction intensities for each peak at all orientations could be satisfactorily reproduced. The extracted variations of diffraction intensity with orientation for (200), (220) and (111) were then used to calculate the ODF of the sample, assuming axial symmetry, with the WIMV algorithm of the BEARTEX package. **Figure 4a-d** presents a comparison for reflection (200) between the experimental intensities (circles and dots), those recalculated from the ODF fitted in the Rietveld package MAUD (dashed lines), and those recalculated from the ODF fitted in BEARTEX (solid lines). Overall, only small differences are observed.

3.3 *Lattice strain analysis*

The X-ray diffraction data were then analyzed to determine strain and stress using the procedure outlined in Singh et al. (1998) and briefly summarized here. Following the convention used in elasticity theory of single crystals (e.g. Nye, 1960), the stress state at the center of the specimen is given by:

$$\sigma_{ij} = \begin{pmatrix} \sigma_1 & 0 & 0 \\ 0 & \sigma_1 & 0 \\ 0 & 0 & \sigma_3 \end{pmatrix} = \begin{pmatrix} \sigma_P & 0 & 0 \\ 0 & \sigma_P & 0 \\ 0 & 0 & \sigma_P \end{pmatrix} + \begin{pmatrix} -t/3 & 0 & 0 \\ 0 & -t/3 & 0 \\ 0 & 0 & 2t/3 \end{pmatrix}, \qquad (2)$$

where $(\sigma_3 - \sigma_1) \equiv t$. t is a measure of the deviatoric stress and is defined as uniaxial stress component (USC) following the nomenclature of (Singh and Kennedy, 1974; Singh and Balasingh, 1977). σ_P is the equivalent hydrostatic pressure.

The d-spacings for a given set of lattice planes measured by X-ray diffraction vary as a function of the angle χ between the compression direction and the diffracting plane normal according to the relation:

$$d_m(hkl) = d_P(hkl)[1 + (1 - 3\cos^2 \chi)Q(hkl)], \quad (3)$$

where $d_m(hkl)$ is the measured *d*-spacing and $d_P(hkl)$ the *d*-spacing under the equivalent hydrostatic pressure σ_P and

$$Q(hkl) = \frac{t}{3}\left[\frac{\alpha}{2G_R(hkl)} + \frac{1-\alpha}{2G_V}\right], \quad (4)$$

where $G_R(hkl)$ and G_V are bounds to the shear modulus of the aggregate under the Reuss (iso-stress) and Voigt (iso-strain) approximations, respectively (Singh et al., 1998). The factor α which lies between 0 and 1, determines the relative weight of isostress (Reuss) and isostrain (Voigt) conditions. It specifies the degree of stress and strain continuity across grains in the sample.

For a cubic material, we have

$$(2G_V)^{-1} = \frac{5}{2}\frac{(S_{11} - S_{22})S_{44}}{[3(S_{11} - S_{12}) + S_{44}]} \quad (5)$$

and

$$\left[2G_R(hkl)\right]^{-1} = S_{11} - S_{12} - 3S\Gamma(hkl), \quad (6)$$

where $S = S_{11} - S_{12} - S_{44}/2$ is a measure of elastic anisotropy, and where the S_{ij} are the single crystal elastic compliances. The orientation factor

$$\Gamma(hkl) = \frac{h^2k^2 + k^2l^2 + l^2h^2}{(h^2 + k^2 + l^2)^2}$$

ranges from 0 for the 200 line to a maximum of 1/3 for 111.

The axial stress, which represents a proxy for the material's strength (e.g. Singh et al., 1998; Kavner, 2003) can be estimated from experimental results using the relation:

$$t = \sigma_3 - \sigma_1 \approx 6G < Q(hkl) >, \quad (7)$$

where G is Hill's average of the Voigt and Reuss bounds to the shear modulus of the aggregate, and $< Q(hkl) >$ is the average of the $< Q(hkl) >$ deduced from the experimental data for the different diffraction lines (Singh et al., 1998).

The variations of the experimental d-spacings of the (111), (200) and (220) planes with χ upon compression and decompression were least-square fitted to Eq. 3 (**Figure 5 a-c**) in order to deduce $d_p(hkl)$ and $Q(hkl)$. In each case we allowed the maximum stress direction to be slightly shifted from δ=0° by introducing an offset in Eq. 3 as it could be observed in the experimental data that the d-spacings minima and maxima were not always perfectly aligned at 0° and 90°. This offset (on the order of 5° to 10°) could only be observed for lattice strains measurements and is not observed in the sample texture (i.e. diffraction intensities). $Q(hkl)$ values were then plotted as a function of Γ and fitted to Eq. (4), which is linear in Γ for the cubic case (**Figure 6**). $<Q(hkl)>$, which represents an estimation of the strength of the sample normalized to the shear modulus ($<Q(hkl)> = t/6G$, from Eq. 7) was calculated from the linear regression. Finally, the fitted slope (m_1) and the ordinate axis value (m_0) was used to calculate elastic anisotropy (A) (**Figure 6**).

$$A = \left(\frac{2C_{44}}{C_{11} - C_{12}}\right) = \frac{3m_0}{3m_0 + m_1} \tag{8}$$

where the C_{ij} are the single crystal elastic moduli of the material.

4. Results

4.1 Rietveld analysis with MAUD

Lattice parameters of $(Mg_{0.40},Fe_{0.60})O$, $(Mg_{0.25},Fe_{0.75})O$, $(Mg_{0.10},Fe_{0.90})O$ were refined for each pressure and composition (**table 1a-d**). We have fixed the uncertainty on the refined unit cell parameters to an average value of ± 0.005 Å, consistent with the precision of peak position determination in our X-ray diffraction experiments ($\sigma(d_{hkl})\sim 10^{-4}$ at beamline 12.2.2 of the Advanced Light Source). The estimated standard deviations on the unit cell parameter calculated in the Rietveld refinement appear largely underestimated because of the many assumptions involved in this whole spectrum fit procedure. The pressure dependence (V/V_0) that we determined for $(Mg_{0.40},Fe_{0.60})O$, $(Mg_{0.25},Fe_{0.75})O$, and $(Mg_{0.10},Fe_{0.90})O$ is in agreement, within estimated uncertainties, with the existing 300 K isothermal equation of state for similar compositions (Jacobsen et al., 2002; Mao et al., 2002) (**Figure 7a-c**).

The principal components of the deviatoric stress tensor (σ_{11}, σ_{22}, σ_{33}) were evaluated using a simple triaxial stress model as part of MAUD refinement procedure, based on estimated bulk and shear moduli (see **section 3**). To account for the typical geometry of stress in the DAC, σ_{33} was refined with $\sigma_{22} = \sigma_{11}$ and $\sigma_{11}+\sigma_{22}+\sigma_{33} = 0$. The maximum principal component of the deviatoric stress tensor (σ_{33}) obtained from the refinements tend to increase and later saturate with increasing pressure and range from 0 to 3 GPa (**tables 1a-d**).

Our texture analysis with the Rietveld approach shows that $(Mg_{0.4}Fe_{0.6})O$, $(Mg_{0.25}Fe_{0.75})O$ and $(Mg_{0.1}Fe_{0.9})O$ deformed in compression in the DAC mainly have a [100] texture as displayed in inverse pole figures (**Figure 8**). **Table 2** presents the minima and maxima of all ODFs calculated in this study. The texture strength *F*2 ranges between 1.7 and 2.3 for $(Mg_{0.4}Fe_{0.6})O$, 1.1 and 1.3 for $(Mg_{0.25}Fe_{0.75})O$ and 1.0 and 1.02 for $(Mg_{0.1}Fe_{0.9})O$. The texture index of MgO determined by Merkel et al. (2002) in a comparable pressure range (0-35 GPa) ranges between 1 and 2.7 in two different experiments.

The volume fraction of the main texture component at [100] (as defined in the experimental section) for all the samples and all pressures is reported in **table 2** and plotted as a function of pressure in **Figure 9**. Its pressure and compositional dependencies are in good agreement with those observed for both *F*2 index and ODF maximum values. The combination of these results shows that the texture strength of magnesiowűstites (a) increases and later saturates with increasing pressure, and (b) weakens with increasing Fe content. One of the experiments (experiment 2) performed on MgO by Merkel et al (2002) shows a weaker pressure dependence of texture strength. One possible reason of this behavior could be found in the sample arrangement used in this second experiment (MgO was loaded as thermal insulator and pressure transmitting medium around Fe).

Texture analysis performed independently by individual fit of peaks confirms that the main texture of magnesiowűstites is at [100]. **Figure 4a-d** presents the intensities of diffraction peak (200) of MgO, $(Mg_{0.4}Fe_{0.6})O$, $(Mg_{0.25}Fe_{0.75})O$ and $(Mg_{0.1}Fe_{0.9})O$ as a function of the angle χ at comparable pressures. The overall variation of amplitude of the diffraction intensities with χ decreases with increasing iron content, such that

$(Mg_{0.1}Fe_{0.9})O$ shows a nearly random distribution. The inverse pole figures obtained with the whole spectrum fit approach (Rietveld method) (**Figure 8 a.1.** and **b.1.**) confirm the results obtained in the inverse pole figures recalculated from the individual peak fits are shown in **Figure 8** (**a.2.** and **b.2.**).

4.2 *Elastic anisotropy and stress*

The axial stress component in the sample can be calculated from the variations of the d-spacings with orientation in the diffraction pattern. In the present analysis, we calculated the average axial stress component $\langle t \rangle$, defined as $6G\langle Q(hkl) \rangle$, where G is the average shear modulus of the aggregate under the Hill approximation. In order to assess effects of plastic deformation, we also evaluated individual stress components using Eq. 4 and the Reuss approximation for (200), (111) and (222) when data for (111) was not available.

The value of $\langle Q(hkl) \rangle$ increases with pressure from 0.03 to 0.06 in $(Mg_{0.40}Fe_{0.60})O$, 0.02 to 0.05 in $(Mg_{0.25}Fe_{0.75})O$, 0.03 to 0.06 in $(Mg_{0.10}Fe_{090})O$ (run 1) and 0.03 to 0.05 in $(Mg_{0.10}Fe_{0.90})O$ (run 2). In general, we find that stress ($6G\langle Q(hkl) \rangle$) increases and later saturates with increasing pressure. It is higher for the MgO samples measured by Merkel et al. (2002) than for the present magnesiowűstite samples (**Figure 10a, Table 3**). For MgO, stresses measured on (222) tend to be larger than stresses on (200). For other compositions, stresses measured on (200) tend to be larger than those measured on (111).

The elastic anisotropy factor *A* for $(Mg_{0.40}Fe_{0.60})O$, $(Mg_{0.25}Fe_{0.75})O$ and $(Mg_{0.10}Fe_{0.90})O$ decreases with increasing pressure and increasing iron content (**Figure 10b, Table 3**). *A* is the ratio of the shear moduli in the (100) and (110) planes in the [100] direction. If *A*=1 the material is elastically isotropic. We find a change of sign of the anisotropy factor of magnesiowűstite at a pressure that depends on composition, leading to an interchange in the direction of fastest and slowest compression and shear wave propagation. For instance, at low pressure, compression waves travel faster along <111>, at high pressure <100> is the fastest direction. The pressure of reversal obtained from the radial diffraction data is in reasonable agreement with simple models based on third order Eulerian strain equations (Davies, 1974) using the ambient pressure elastic moduli of Jacobsen et al. (2002) and the pressure derivatives of Bonczar and Graham (1982) (**Figure 10b**).

5. Discussion

5.1 Lattice preferred orientation

For all examined compositions, our experiments document the development of a main texture component at [100] with increasing pressure. The [100] texture is due to {110}<1-10> slip as explored previously (Wenk et al. 1989, Merkel et al. 2002). If {110}<1-10>, {111}<1-10> and {100}<011> slip systems were all active simultaneously, the maximum in the inverse pole figure would be a girdle between [110]

and [100]. Textures we obtain in $(Mg_{0.1}Fe_{0.9})O$ are particularly weak and sometimes show other maxima than [100]. However, the intensity of those secondary maxima are weak and depend on the fitting method.

In order to study the influence of iron on (Mg,Fe)O we compared our results with those of pure MgO as a reference under similar experimental conditions (Merkel et al., 2002). Indeed, we find that pure MgO has the same main texture component at [100] as our magnesiowűstite samples (**Figure 8**). The texture strength tends to decrease with increasing iron content (**Table 2** and **Figures 8, 9**). With increasing iron content, bonding becomes less ionic and the strength decreases. This could result in lower stacking fault energy for the slip system {110}<1-10) (Miranda and Scandolo, 2005). Another explanation could be that in iron-rich, more compressible, magnesiowűstites a larger portion of strain is accommodated elastically. The observed broadening of the diffraction lines in all three magnesiowűstite compositions with increasing pressure, may also be an expression of such heterogeneous elastic strain, probably because of higher dislocations densities.

$(Mg_{0.80}Fe_{0.20})O$ up to 300 MPa and 1400 K by Stretton et al. (2001) show [100] and [110] texture in analyses using the EBSD technique. The samples at higher temperature (1400 *K*) and larger grain size and those at lower temperature (1200 *K*) and smaller grain size, show a stronger texture at [110], which broadens towards [100] with a minimum at [111]. The texture is only slightly stronger for the sample deformed at lower temperature (1200 K). This suggests that temperature plays a relevant role on deformation mechanisms of magnesiowűstite, similar to isostructural halite (Carter and Heard, 1970).

Heidelbach et al. (2003) studied texture evolution as function of strain, observing a change from a dislocation creep texture at low strains to a recrystallization texture at high strains. With increasing strain the texture components in the following order become more evident: {111}<110>, {100}<110> and finally at the highest strains the texture component {112}<110>. The overall observed texture strengths in this study are relatively low compared to the high strains. This is explained with the subgrain rotation recrystallization, weakening strong maxima due to rotation of the crystals.

Another aspect that has to be considered in order to understand the deformation behavior of magnesiowűstites is the complex defect structure associated with very high Fe contents. The less ionic bonding strength in (Mg,Fe)O and the probably existing vacancies in the (Mg,Fe)O crystal structure (Jacobsen et al., 2002) might increase the density of dislocations (Luecke and Kohlstedt, 1988; Pulliam, 1963; Heidelbach et al., 2003).

Finally, we cannot neglect that grain size, grain shape, grain distribution, configuration of the existing phases, deformation history etc. in the sample can play a role in the deformation process.

5.2 *Orientation of stress in the DAC*

For each pressure, we could observe a slight offset in the maximum stress direction in the measured d-spacings. This indicates that the maximum stress applied to the sample is not always aligned with the anvil directions but can be shifted by a few

degrees. This is probably related to details of the experimental setup such as diamond alignment and sample loading. This has been also observed on other samples in DAC radial diffraction experiments (Merkel et al 2005, Merkel and Yagi 2005b). Interestingly, this offset is not observed in the measured diffraction intensities, indicating that the texture and plastic deformation of the sample is indeed axisymmetric. It should be noted that this can be problematic for whole profile Rietveld refinements in MAUD as this stress geometry can not be readily refined.

5.3 *Effect of plasticity on the deduced anisotropy*

In order to better quantify the combined effects of pressure increase and Fe-Mg substitution on the elastic anisotropy in magnesiowűstites we have compared our experimental values of the anisotropy factor (*A*), with model anisotropies calculated from low-pressure single-crystal elasticity data (Jackson and Khanna, 1990; Sinogeikin and Bass, 2000; Jacobsen et al., 2002, 2004) extrapolated using Eulerian finite strain equations (Davies, 1974). The model agrees reasonable well with our experimental results (**Figure 10b**). These results indicate that the lattice strain theory (Singh et al, 1998) can be applied to obtain a first estimate of the anisotropies of cubic materials.

In recent years, models based on a combination of polycrystal plasticity and lattice strain theories predicted that for materials such as MgO, stresses deduced from lattice strain measurements on (111) should become over 50% greater than deduced from (200), once plastic deformation is activated (Weidner et al. 2004). This model appears to

agree with the results on MgO of Merkel et al. (2002). However, it contradicts our measurements for iron-rich magnesiowűstites for which the stress measured on (200) is larger than that measured on (111) (**Figure 10a**). Our experiments do indicate an (hkl)-dependence of stress but much lower than predicted by Weidner et al. (2004). It should be noted that elasto-plastic models such as those used by Weidner et al. (2004) and Li et al. (2004) depend on a number of parameters, such as the combination of active slip system and the elastic anisotropy of the material. Our results indicate that the combination of parameters used in those models were optimized to match the data measured for MgO. In particular, elastic anisotropy in magnesiowustite changes greatly with increasing iron content and therefore the models of Weidner et al. (2004) and Li et al. (2004) may not apply directly. The evolution of elastic anisotropy with pressure and composition deduced from this study is in fairly good agreement with other techniques (**Figure 10b**). This indicates that the radial diffraction data can be used to extract trends of variation of anisotropies with composition. However, as pointed out by Weidner et al. (2004) and Li et al. (2004), the absolute values obtained should be treated with caution.

6. Conclusion

Axial deformation experiments on $(Mg_{0.4}Fe_{0.6})O$, $(Mg_{0.25}Fe_{0.75})O$ and $(Mg_{0.1}Fe_{0.9})$ with the DAC show the development of a [100] texture. The comparison between the lattice preferred orientation in our (Mg,Fe)O samples with those observed in pure MgO, both at room temperature, suggest that the {1-10}<110> is the main active slip system at

these conditions. However, the weakening of texture with increasing iron content is significant.

Stress measured in our magnesiowustite samples is significantly lower than previously measured in MgO (Merkel et al. 2002). Contrary to models based on polycrystal plasticity and lattice strain theories and applied to MgO (Weidner et al. 2004), we find that for iron-rich compositions, the effective stress measured on (111) is lower than that measured on (200). Elasto-plastic models such as the ones used in Weidner et al. (2004) and Li et al. (2004) depend on a number of parameters, such as the combination of active slip system and the elastic anisotropy of the material, and our results underline that they can only be used to interpret and analyze the experiments they were designed for.

Finally, the elastic anisotropy deduced from the X-ray diffraction data decreases with increasing pressure and iron content, in a agreement with model bases on low-pressure single-crystal elasticity data (Jackson and Khanna, 1990; Sinogeikin and Bass, 2000; Jacobsen et al., 2002, 2004) extrapolated using Eulerian finite strain equations (Davies, 1974). This indicates that the radial diffraction data could be used to extract trends of variation of anisotropies with composition.

Acknowledgement

C.E.T. thanks the DFG (TO257/3-1) for financial support. This work was supported by NSF and CDAC. We are appreciative for access to the facilities at APS and ALS. We acknowledge help by M. Kunz and L. Miyagi with the experiment and Ivan Lonardelli, Gloria Ischia, Ingwar Huensche and Jenny Pehl with MAUD data analysis and fruitful

discussions. Comments on the manuscript by reviewers were very helpful. We also thank R. Jeanloz for providing some of the samples used in the experiments.

References

Anderson OL, Isaak DG Yamamoto S (1989) Anharmonicity and the equation of state for gold. J Appl Phys 65: 1534-1543

Andrault D (2001) Evaluation of (Mg,Fe) partitioning between silicae perovskite and magnesiowűstite up to 120 GPa and 2300 K. J Geophys Res 106: 2079-2087

Badro J, Fiquet G, Guyot F, Rueff JP, Struzhkin VV, Vankó G, Monaco G (2003) Iron partitioning in Earth s mantle: toward a deep lower mantle discontinuity. Science 300: 789-791

Bonczar LJ Graham EK (1982) The pressure and temperature dependence of the elastic properties of polycrystal magnesiowűstite. J Geophys Res 87: 1061-1078

Bunge HJ (1982) Texture analysis in materials science. Butterworths, London, pp 593

Carter NL, Heard HC (1970) Temperature and rate-dependent deformation of halite. Amer J Sci 269: 193-249

Cohen RE, Mazin II, Isaak DG (1997) Magnetic collapse in transition metal oxides at high pressure: implications for the Earth. Science 275: 654 -657

Davies GF (1974) Effective elastic moduli under hydrostatic stress I. Quasi harmonic theory. J Phys Chem Sol 35: 1513-1520

Dubrovinsky LS, Dubrovinskaia NA, Saxena SK, Annersten H, Halenius E, Harryson H, Tutti F, Rekhi S, Le Bihan T (2000) Stability of ferropericlase in the lower mantle. Science 289: 430-432

Dubrovinsky LS, Dubrovinskaia N, Annersten H, Halenius E, Harrison H (2001) Stability of $(Mg_{0.5}Fe_{0.5})O$ and $(Mg_{0.8}Fe_{0.2})O$ magnesiowűstites in the lower mantle. Eur J Mineral 13: 857-861

Dubrovinsky LS, Dubrovinskaia N, Kantor I, McCammon C, Crichton W, Urusov V (2005) Decomposition of ferropericlase $(Mg_{0.80}Fe_{0.20})O$ at high pressures and temperatures. J Alloys Comp 390: 41-45

Duffy TS, Shen G, Heinz DL, Shun J, Me Y, Mao HK (1999) Lattice strains in gold and rhenium under non-hydrostatic compression to 37 GPa. Phys Rev B 60: 15063-15073

Hammersley, A.P. (1998) FIT2D Reference Manual (European Synchrotron Radiation Facility, Grenoble, France), Version 4.0

Heidelbach F, Stretton I, Langenhorst F, Mackwell S (2003) Fabric evolution during high shear-strain deformation of magnesiowűstite. J Geophys Res B 108: 2154

Ischia G, Wenk HR, Lutterotti L, Berberich (2005) Quantitative Rietveld texture analysis of zirconium from single synchrotron diffraction images. J Appl Cryst 38: 377-380

Jackson I and Khanna SK (1990) Elasticity, shear-mode softening and high-pressure polymorphism of wuestite ($Fe_{1-x}O$). J Geophys Res 95: 21671-21685

Jacobsen SD, Reichmann HJ, Spetzler HA, Mackwell SJ, Smyth JR, Angel RJ McCammon C (2002) Structure and elasticity of single-crystal (Mg,Fe)O and a new method of generating shear waves for gigahertz ultrasonic interferometry. J Geophys Res 107 (B2): 1-14

Jacobsen SD, Spetzler HA, Reichmann HJ, Smyth JR (2004) Shear waves in the diamond-anvil cell reveal pressure-induced instability in (Mg,Fe)O. Proceedings of the National Academy of Sciences USA 101: 5867-5871

Karato S (1998a) Seismic anisotropy in the deep mantle and the geometry of mantle convection. Pure Appl Geophys 151: 565-587

Karato SI (1998b) Some remarks on the origin of seismic anisotropy in D'' layer. Earth Planets Space 50: 1019-1028

Karki B, Stixrude L, Clark S, Warren M, Ackland G and Crain J (1997) Elastic properties of orthorhombic $MgSiO_3$ perovskite at lower mantle pressures. Amer Mineral 82:635-638.

Kavner A (2003) Elasticity and strength of hydrous ringwoodite at high pressure. Earth Planet Sci Lett 214: 645-654

Kondo T, Ohtani E, Hirao E, Yagi T Kikegawa T (2004) Phase transitions of (Mg,Fe)O at megabar pressures Physics of the Earth Planet Inter 143-144: 201-213

Li L, Weidner DJ, Raterron P, Chen J and Vaughan MT (2004) Stress measurements of deforming olivine at high pressure. Physics of the Earth and Planetary Interiors 143-144: 357-367

Lin JF, Heinz DL, Mao HK, Hemley RJ, Devine JM, Li J, Shen G (2003) Stability of magnesiowűstite in earth's lower mantle. Proc Nat Acad Sc 8: 4405-4408

Lin JF , Struzhkin VV, Jacobsen SD, Hu MY, Chow P, Kung J, Liu H, Mao HK, Hemley RJ (2005) Spin transition of iron in magnesiowüstite in the Earth s lower mantle. Nature 436: 377-380

Lonardelli I, Wenk H.-R., Lutterotti L, Goodwin M (2005) Texture analysis from synchrotron diffraction images with the Rietveld method: Dinosaur tendon and salmon scale. J Synchr Rad 12: 354-360

Luecke W and Kohlstedt DJ (1988) Kinetics of the internal oxidation of (Mg,Fe)O solid solutions. J Am Ceram Soc 71: 189-196

Lutterotti L, Matthies S, Wenk HR (1999) MAUD: a friendly Java program for materials analysis using diffraction. Int U Crystallogr Comm Powder Diffraction Newsletter 21: 14-15

Madi K, Forest S, Cordier P and Boussuge M (2005) Numerical study of creep in two-phase aggregates with a large rheology contrast: Implications for the lower mantle. Earth and Planetary Science Letters 237: 223-238

Mao HK, Shu J, Fei Y, Hu J Hemley RJ (1997) Multivariable dependence of Fe-Mg partitioning in the lower mantle. Science 278: 2098-2100

Mao W, Shu J, Hu J, Hemley R, Mao HK (2002) Displacive transition in magnesiowűstite. J Phys Condens Matter 14: 11349-11354

Matthies S, Vinel GW (1982) On the reproduction of the orientation distribution function of textured samples from reduced pole figures using the concept of conditional ghost correction. Phys Stat Sol 112 : K111-114

McCammon CA (1993) Effect of pressure on the composition of the lower mantle end member FexO. Science 259: 66-68

Merkel S,Wenk HR, Shu J, Shen G Gillet P, Mao HK, Hemley RJ (2002) Deformation of polycrystalline MgO at pressures of the lower mantle. J Geophys Res 107: 2271

Merkel S, Shu J, Gillet P, Mao HK, Hemley RJ (2005) X-ray diffraction study of the single crystal elastic moduli of e-Fe up to 30 GPa. J. Geophys. Res. 110: B05201

Merkel S, Yagi T (2005a) X-ray transparent gasket for diamond anvil cell high pressure experiments. Review of scientific instruments 76: 046109

Merkel S, Yagi T (2005b) Effect of plasticity on lattice strains in polycrystalline materials deformed under high pressure: application to hcp-Co. J. Phys. Chem. Solids. Submitted.

Miranda CR, Scandolo S (2005) Computational materials science meets geophysics: dislocations and slip planes of MgO. Comp. Phys. Comm. 169: 24

Nye JF (1960) Physical properties of crystals (Oxford: Clarendon), pp 322

Pulliam GR (1963) Decorated dislocations in magnesia crystals. J Am Ceram Soc, 46: 202-206

Richet P, Mao HK, Bell PM (1989) Bulk moduli of magnesiowűstites from static compression measurements. J Geophys Res 94, 3037-3045

Sherman D M (1988) in Structural and Magnetic Phase Transitions in Minerals (eds Ghose, S., Coey, J. M. D. & Salje, E.) 113 -118 (Springer, New York).

Sherman DM (1991) The high-pressure electronic structure of magnesiowüstite (Mg,Fe)O: applications to the physics and chemistry of the lower mantle. J. Geophys. Res. 96: 14299-14312

Sherman DM, Jansen, HJF (1995) First-principles predictions of the high-pressure phase transition and electronic structure of FeO: implications for the chemistry of the lower mantle and core. Geophys. Res. Lett. 22: 1001 -1004

Singh AK and Kennedy GC (1974) Uniaxial stress component in tungsten carbide anvil high-pressure X-ray cameras. J Appl Phys 45: 4686

Singh AK and Balasingh C (1977) Uniaxial stress component in diamond anvil high-pressure X-ray cameras. J Appl Phys 48: 5338

Singh AK, Balasingh C, Mao HK, Hemley RJ and Shu, J (1998) Analysis of lattice strains measured under non-hydrostatic pressure. J Appl Phys 83: 7567-7575

Sinogeikin SV and Bass JD (2000) Single-crystal elasticity of pyrope and MgO to 20 GPa by Brillouin scattering in the diamond cell. Physics of the Earth Planet Inter 120: 43-62

Speziale S, Milner A, Lee VE, Clark SM, Pasternak MP, Jeanloz R (2005) Iron spin transition in Earth's mantle. Proc Nat Acad Sc: in press.

Stretton I, Heidelbach F, Mackwell SJ Langenhorst F (2001) Dislocation creep of magnesiowűstite ($Mg_{0.8}Fe_{0.2}O$). Earth Planet Sci Lett 194: 229-240

Weidner DJ, Li L, Davis M and Chen J (2004) Effect of plasticity on elastic modulus

measurements. Geophys Res Lett 31: 1-4

Wenk HR, Canova GR, Molinari A, Mecking HH (1989) Texture development in halite: comparison of Taylor model and self-consistent theory. Acta Metall 37: 2017-2029

Wenk HR, Matthies S, Donovan J, Chateigner D (1998) BEARTEX, a Windows-based program system for quantitative texture analysis. J Appl Cryst 31: 262-269

Wentzcovitch RM, Karki BB, Karato S, Silvera CRSD (1998) High pressure elastic anisotropy of MgSiO3 and geophysical implications. Earth Planet Sci Lett 164: 371-378

Yagi T, Suzuki T, Akimoto S (1985) Static compression of wüstite ($Fe_{0.98}O$) to 128 GPa. J Geophys Res 90: 8784-8788

Yamazaki D Karato SI (2001) Some mineral physics constraints on the rheology and geothermal structure of Earth's lower mantle. Am Miner 86: 385-391

Yamazaki D, Karato SI (2002) Fabric development in (Mg,Fe)O during large strain, shear deformation: implications for seismic anisotropy in Earth's lower mantle. Physics of the Earth and Planetary Interiors 131: 251-267

Figure Captions

Figure 1. Representative diffraction patterns of magnesiowűstite, $(Mg_{0.4}Fe_{0.6})O$ (**1a**) and $(Mg_{0.1}Fe_{0.9})O$ (**1b**), both recorded at 13 GPa.

Figure 2. Selected diffraction profiles for $(Mg_{0.4}Fe_{0.6})O$ (**2a**) and $(Mg_{0.1}Fe_{0.9})O$ (**2b**) at 13 GPa. Dotted lines are experimental data, solid lines are results from full profile refinement with the Rietveld technique. The profiles at 0° and 180° are in the compression direction and the profiles at 90° are in the extension direction. The 0° spectrum in **Figure 2b** is not shown as it corresponds to the position of the beam-stop. Note the variations in peak positions and peak intensities with orientation, which are related to deviatoric stress and texture. A broadening of the peaks is observed. Diffraction lines of the sample are labeled on the figure. The diffraction peaks of the Au pressure standard are also indicated.

Figure 3. (100) pole figures of $(Mg_{0.4}Fe_{0.6})O$ smoothed with 11° Gauss filter without imposing symmetry (**3a**) and with imposed cylindrical symmetry (**3b**) at 13 GPa. Equal area projection. Four-fold symmetry in Fig 3a is an artifact resulting from the pole figure coverage.

Figure 4a-d. Variation of the diffraction intensities with χ for **4a.** pure MgO, **4b.** $(Mg_{0.4}Fe_{0.6})O$, **4c.** $(Mg_{0.25}Fe_{0.75})O$ and **4d.** $(Mg_{0.1}Fe_{0.9})O$ at about 13 GPa. Open (1. experiment) and full circles (2. experiment) are experimental data and solid and dashed lines are recalculated from the ODF fitted to the experimental intensities with WIMV as implemented in BEARTEX (solid lines) and ODF fitted with MAUD using the EWIMV algorithm (dashed lines), respectively.

Figure 5. $d_m(111)$ (**5a**), $d_m(200)$ (**5b**) and $d_m(220)$ (**5c**) versus χ for $(Mg_{0.1}Fe_{0.9})O$ at 13 GPa. Circles are experimental data and solid lines are fits of lattice strain equations.

Figure 6. $Q(hkl)$ versus $I(hkl)$ for $(Mg_{0.1}Fe_{0.9})O$ at 4, 13 and 18 GPa.

Figure 7. V/V_0 versus pressure for $(Mg_{0.4}Fe_{0.6})O$ (**7a**), $(Mg_{0.25}Fe_{0.75})O$ (**7b**) and $(Mg_{0.1}Fe_{0.9})O$ (**7c**).

Figure 8. Inverse pole figures for different compositions in the MgO-FeO series: **8a.1.** MgO (experiment 1 and 2), $(Mg_{0.4}Fe_{0.6})O$, $(Mg_{0.25}Fe_{0.75})O$ recalculated from MAUD using EWIMV algorithms. **8a.2.** The same as 8a.1. recalculated with WIMV as implemented in BEARTEX from the single peak fits. **8b.1.** Inverse pole figures for $(Mg_{0.1}Fe_{0.9})O$ (runs 1 and 2) from MAUD using the EWIMV algorithms. **8b.2.** The same as 8b.1. recalculated with WIMV as implemented in BEARTEX from the single peak fits. Because of the weaker texture, the $(Mg_{0.1}Fe_{0.9})O$ composition is presented with a different gray scale. Equal projection area.

Figure 9. 100 texture component (Vol%) versus pressure for different compositions in the MgO-FeO solid solution series. The radius of the spherical texture component was chosen at 20°. Data for $(Mg_{0.1}Fe_{0.9})O$ (open and closed squares), $(Mg_{0.25}Fe_{0.75})O$ (crosses), $(Mg_{0.4}Fe_{0.6})O$ (circles), and MgO (open and closed triangles) are shown on the figure. Lines are guide to the eye through the experimental data and the star symbol indicates the value that would be obtained for a random texture.

Figure 10a-b. 10a. Mean stress (6G<Q(hkl)>), and effective stresses deduced from measurements on (111) and (200) vs. pressure for all samples as a function of pressure. For the measurements on MgO, effective stresses were calculated on (222) and (200) as no data for (111) was available. For clarity, measurements of MgO (experiment 1) and $(Mg_{0.1}Fe_{0.9})O$ (run1) were not included in the figure but they do not differ significantly. . **10b.** Elastic anisotropy in magnesiowűstite expressed with the Zener ratio $A = 2C_{44}/(C_{11}-C_{12})$ as a function of pressure. Results deduced from the x-ray data under the Reuss limit are compared with models based on data from literature (Jackson and Khanna, 1990; Sinogeikin and Bass, 2000; Jacobsen et al., 2002; 2004) (dashed lines).

Tables

Sample $(Mg_{0.4}Fe_{0.6})O$	**a_{MW}[Å] (± 0.005)**	**V/V_0**	**σ_{33} [GPa]**	**gold a[Å]**	**P[GPa]**
4060_2_004	4.243	0.980	-0.5	4.048	4
4060_2_005	4.215	0.961	-1.5	4.018	9
4060_2_006	4.197	0.948	-1.7	4.002	11
4060_2_009	4.175	0.934	-1.3	3.974	16
4060_2_011	4.144	0.913	-2.5	3.948	22
4060_2_013	4.116	0.895	-2.9	3.925	27
4060_2_015	4.099	0.883	-2.6	3.912	30
4060_2_016	4.086	0.875	-2.6	3.901	33
4060_2_018	4.075	0.868	-3.0	3.884	37

(a)

Sample $(Mg_{0.25}Fe_{0.75})O$	**a_{MW} [Å] (± 0.005)**	**V/V_0**	**σ_{33} [GPa]**	**gold a[Å]**	**P[GPa]**
2575_003	4.265	0.988	-0.1	4.067	2
2575_017	4.243	0.973	-0.7	4.048	4
2575_019	4.230	0.964	-1	4.038	6
2575_027	4.188	0.935	-1.3	4.011	10
2575_028	4.162	0.918	-1.4	3.978	16

(b)

Sample $(Mg_{0.1}Fe_{0.9})O$	**a_{MW} [Å] (± 0.005)**	**V/V_0**	**σ_{33} [GPa]**	**gold a[Å]**	**P[GPa]**
1090_005	4.258	0.974	-1	4.047	4
1090_006	4.197	0.933	-1.4	3.994	13
1090_007	4.167	0.913	-1.8	3.968	18

(c)

Sample $(Mg_{0.1}Fe_{0.9})O$	**a_{MW} [Å] (± 0.005)**	**V/V_0**	**σ_{33} [GPa]**	**P[GPa]**
1090_2_006	4.262	0.977	-1.1	4
1090_2_008	4.191	0.929	-1.6	12

(d)

Table 1.a-d. Unit cell parameters of (a) $(Mg_{0.4}Fe_{0.6})O$, (b) $(Mg_{0.25}Fe_{0.75})O$, (c) $(Mg_{0.1}Fe_{0.9})O$ (run 1) (d) $(Mg_{0.4}Fe_{0.6})O$ (run 2). Principal stresses components obtained from the MAUD refinements.

Sample $(Mg_{0.4}Fe_{0.6})O$	**ODF[1] min max [m.r.d.]**	**ODF[2] min max [m.r.d.]**	***F*2**	**Vol-% component**
4060_2_004	0.35 4.25			7.76
4060_2_005	0.41 4.32	0.39 3.96	1.44	11.18
4060_2_006	0.32 3.08	0.79 1.23	1.47	11.65
4060_2_009	0.37 5.23	0.30 6.03	1.96	15.30
4060_2_011	0.04 7.82	0.41 5.21	1.91	14.93
4060_2_013	0.26 5.82	0.38 5.05	1.89	15.05
4060_2_015	0.23 5.73	0.43 5.44	1.89	14.36
4060_2_016	0.31 5.27	0.35 6.16	2.00	15.92
4060_2_018	0.20 6.89	0.44 5.87	2.07	16.40

(a)

Sample $(Mg_{0.25}Fe_{0.75})O$	**ODF[1] min max [m.r.d.]**	**ODF[2] min max [m.r.d.]**	***F*2**	**Vol-% component**
2575_003	0.53 2.06	0.47 1.73	1.04	5.19
2575_017	0.36 1.99	0.43 2.25	1.16	8.18
2575_019	0.33 2.30	0.38 2.24	1.15	8.32
2575_027	0.36 2.15	0.40 2.17	1.18	7.70
2575_028	0.62 1.79	0.33 1.60	1.13	5.99

(b)

Sample $(Mg_{0.1}Fe_{0.9})O$	**ODF[1] min max [m.r.d.]**	**ODF[2] min max [m.r.d.]**	***F*2**	**Vol-% component**
1090_005	0.83 1.13	0.90 1.13	1.00	1.42
1090_006	0.82 1.14	0.79 1.23	1.01	2.12
1090_007	0.83 1.13	0.63 1.17	1.02	2.91

(c)

Sample $(Mg_{0.1}Fe_{0.9})O$	**ODF[1] min max [m.r.d.]**	**ODF[2] min max [m.r.d.]**	***F*2**	**Vol-% component**
1090_2_006	0.75 1.14	0.92 1.09	1.00	0.82
1090_2_008	0.48 1.35	0.59 1.21	1.02	3.27

(d)

Table 2a-d. Texture index *F*2, minima and maxima of the ODF, and principal pole figure 100 with imposing cylindrical symmetry. (a) $(Mg_{0.4}Fe_{0.6})O$, (b) $(Mg_{0.25}Fe_{0.75})O$, (c) $(Mg_{0.1}Fe_{0.9})O$ (run 1) and (d) $(Mg_{0.1}Fe_{0.9})O$ (run 2).

[1] Minima and maxima of the ODF recalculated with WIMV as implemented in BEARTEX from the single peak fits.

[2] Minima and maxima of the ODF recalculated from MAUD using the EWIMV algorithms. The ODF were smoothed using a Gaussian filter of width of 11°. The radius of the texture components were set to 20°.

MgO (experiment 1)						
***P*[GPa]**	***t*(222)**	***t*(200)**	**<*t*>**	***A*[2C_{44}/(C_{11}-C_{12})]**	**ODF Min Max**	***F*2**
1.9	1.5	1.7	1.7	1.674	0.91 1.10	1.00
2.4	2.0	3.0	2.7	1.681	0.89 1.19	1.01
3.1	3.0	2.7	3.1	1.508	0.87 1.26	1.01
5.3	5.6	5.1	5.5	1.252	0.70 2.20	1.11
7.0	5.9	5.5	6.0	1.058	0.63 2.96	1.24
9.5	7.1	6.1	6.8	0.984	0.52 3.78	1.41
11.6	7.0	6.0	6.6	0.987	0.52 3.81	1.41
20.3	8.1	6.4	7.1	0.885	0.22 6.84	2.17
30.3	10.3	9.6	9.5	0.912	0.27 6.46	2.25
35.5	9.4	9.5	8.6	1.071	0.27 6.46	2.25
MgO (experiment 2)						
***P*[GPa]**	***t*(222)**	***t*(200)**	**<*t*>**	***A*[2C_{44}/(C_{11}-C_{12})]**	***ODF Min Max***	***F2***
1.5	2.0	2.0	2.1	1.371		
5.1	4.8	3.8	4.3	0.991	0.71 2.00	1.09
7.5	8.6	6.0	7.5	0.910	0.61 2.15	1.14
11.0	9.8	7.0	8.5	0.869	0.53 2.76	1.26
17.4	9.5	6.8	8.0	0.870	0.52 2.78	1.26
18.3	8.7	6.9	7.7	0.931	0.48 2.57	1.24
20.2	9.0	7.2	7.8	0.960	0.40 2.34	1.21
23.0	10.5	7.3	8.6	0.844	0.53 2.58	1.24
23.9	9.1	7.6	8.3	0.836	0.46 2.80	1.27
27.0	9.6	7.9	8.4	0.852	0.40 2.74	1.26
29.8	10.6	9.5	9.7	0.895	0.47 2.81	1.27

$(Mg_{0.4}Fe_{0.6})O$				
***P*[GPa]**	***t*(111)**	***t*(200)**	**<*t*>**	$A[2C_{44}/(C_{11}-C_{12})]$
4	2.1	1.9	2.1	0.923
9	1.9	1.9	2.0	0.810
11	2.3	2.3	2.3	0.739
16	1.8	1.9	1.9	0.637
22	3.2	3.7	3.3	0.572
27	3.7	4.7	3.9	0.530
30	2.8	4.3	3.3	0.578
33	4.5	5.6	4.7	0.412
37	4.2	6.0	4.7	0.406
$(Mg_{0.25}Fe_{0.75})O$				
4	0.9	1.1	1.0	1.152
6	1.2	1.5	1.4	0.953
10	2.4	2.7	2.5	0.676
16	2.2	3.2	2.6	0.588
$(Mg_{0.1}Fe_{0.9})O$ (run1)				
4	1.6	1.4	1.5	0.651
13	1.9	2.1	2.0	0.449
18	2.2	2.8	2.5	0.360
$(Mg_{0.1}Fe_{0.9})O$ (run2)				
4	1.9	1.7	1.8	0.658
12	1.3	1.9	1.5	0.410

Table 3. Values of effective stresses deduced from the X-ray data on (111) and (200), mean stress value ($\langle t \rangle = 6G\langle Q(hkl)\rangle$), and elastic anisotropy for all compositions studied here along with the MgO results of Merkel et al. (2002). For MgO, minima and maxima of the ODF were deduced from experimental ODF calculated with WIMV and smoothed using a Gaussian filter of width of 11º, as implemented in BEARTEX.

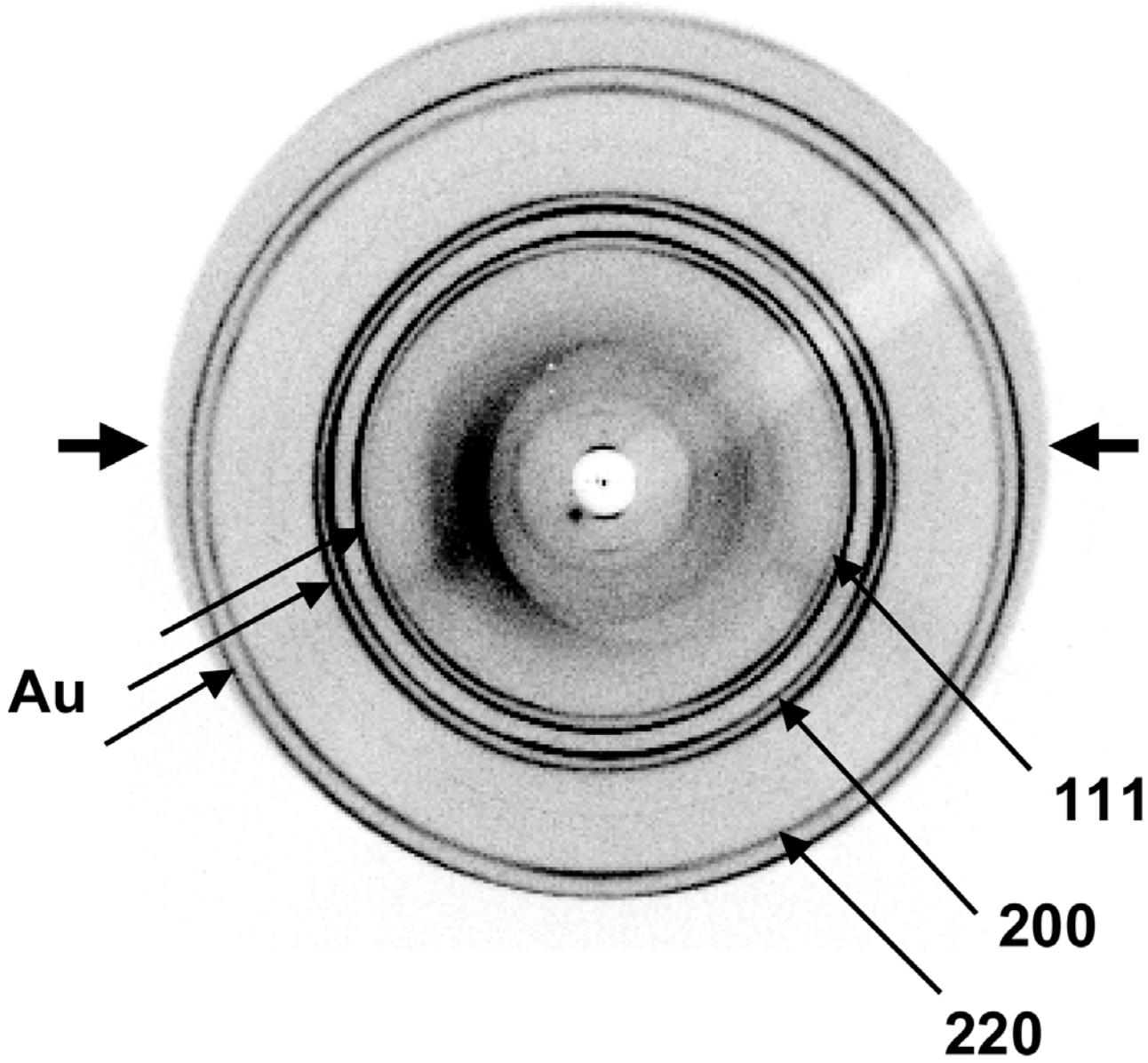

(a)

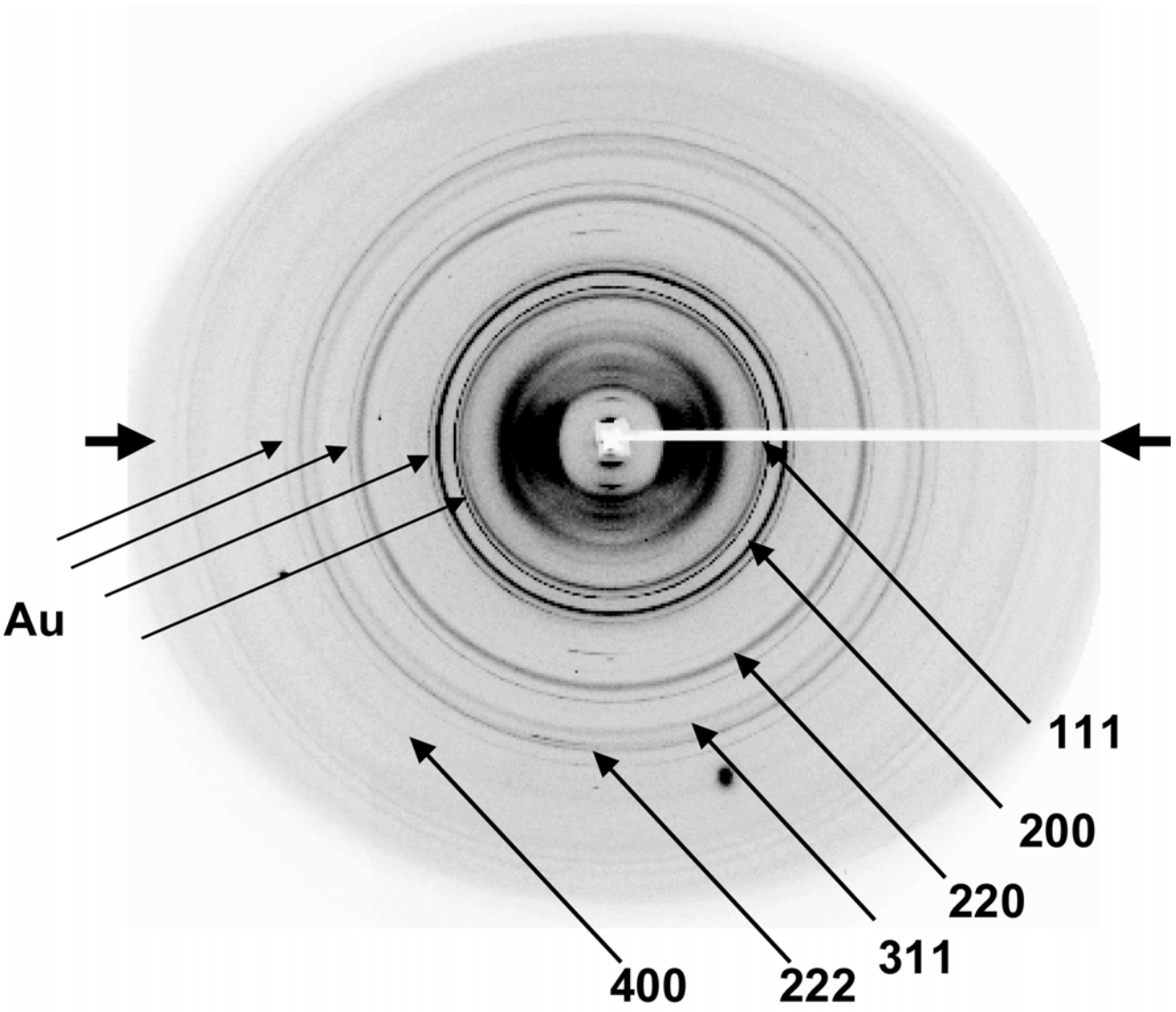

(b)
Figure 1 a-b

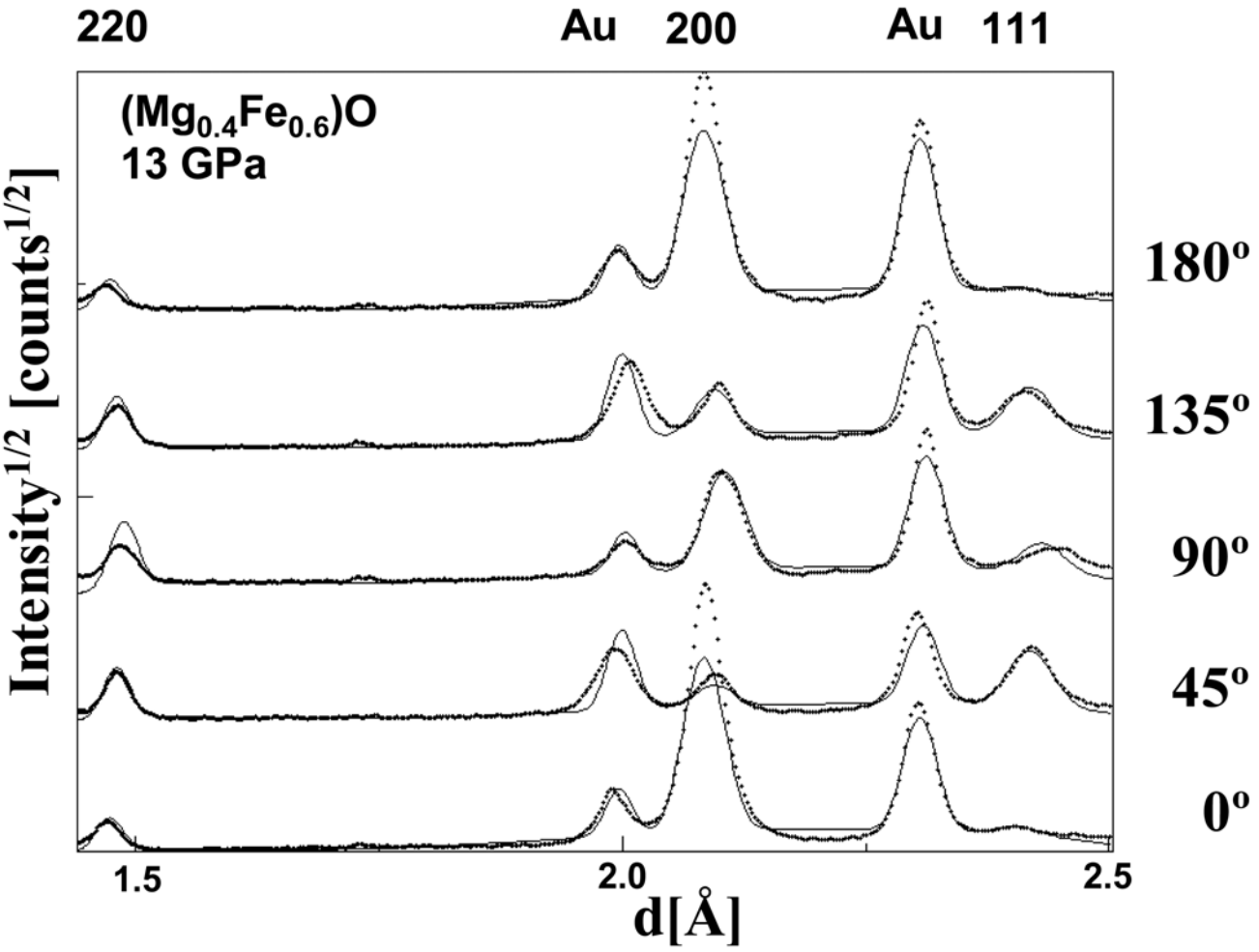
220
Au 200
Au 111
(Mg0.4Fe0.6)O
13 GPa
180°
135°
90°
45°
0°
Intensity1/2 [counts1/2]
1.5
2.0
2.5
d[Å]

(a)

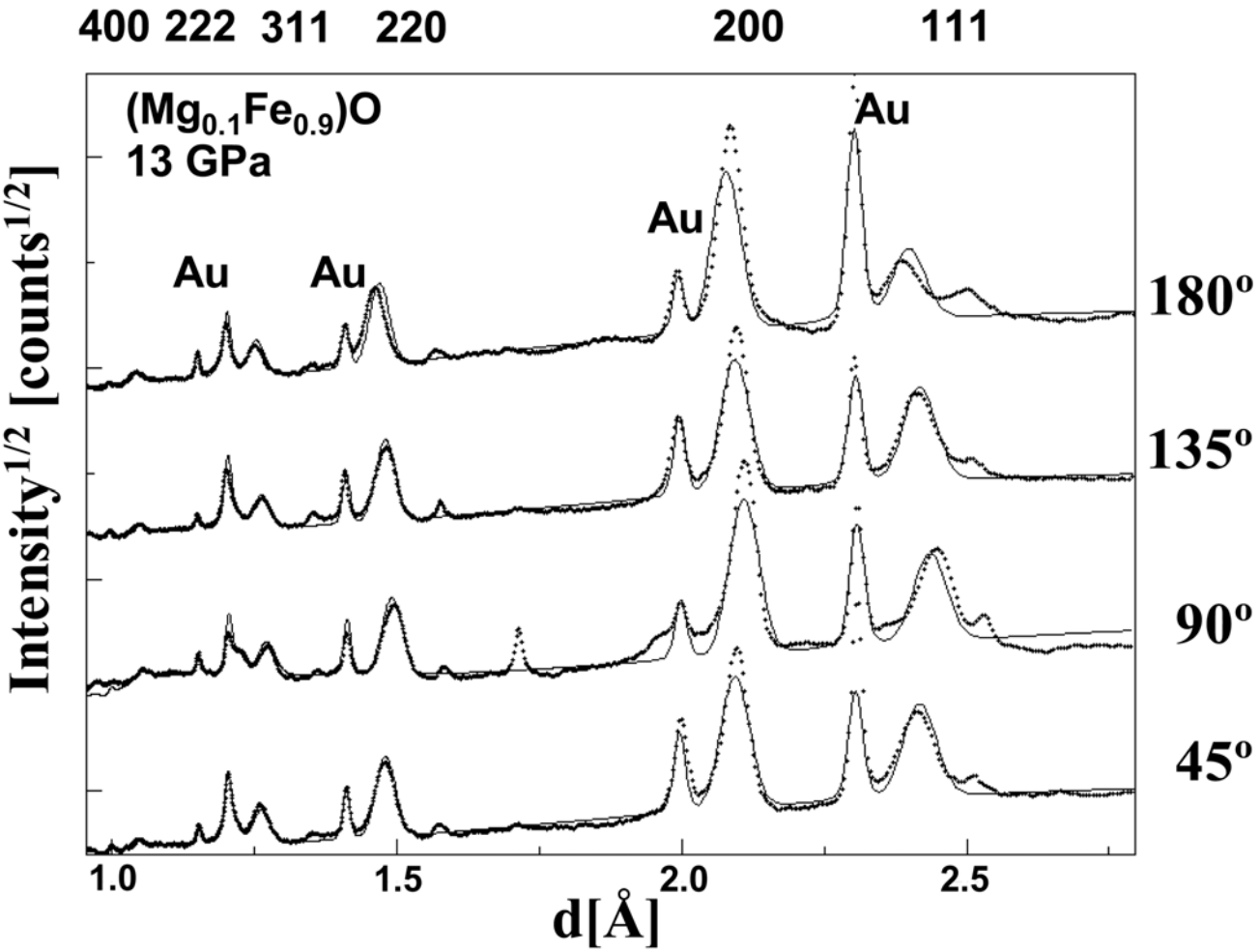
400 222 311 220
200
111
(Mg0.1Fe0.9)O
13 GPa
Au
Au
Au
Au
180°
135°
90°
45°
Intensity1/2 [counts1/2]
1.0
1.5
2.0
2.5
d[Å]

(b)
Figure 2a-b

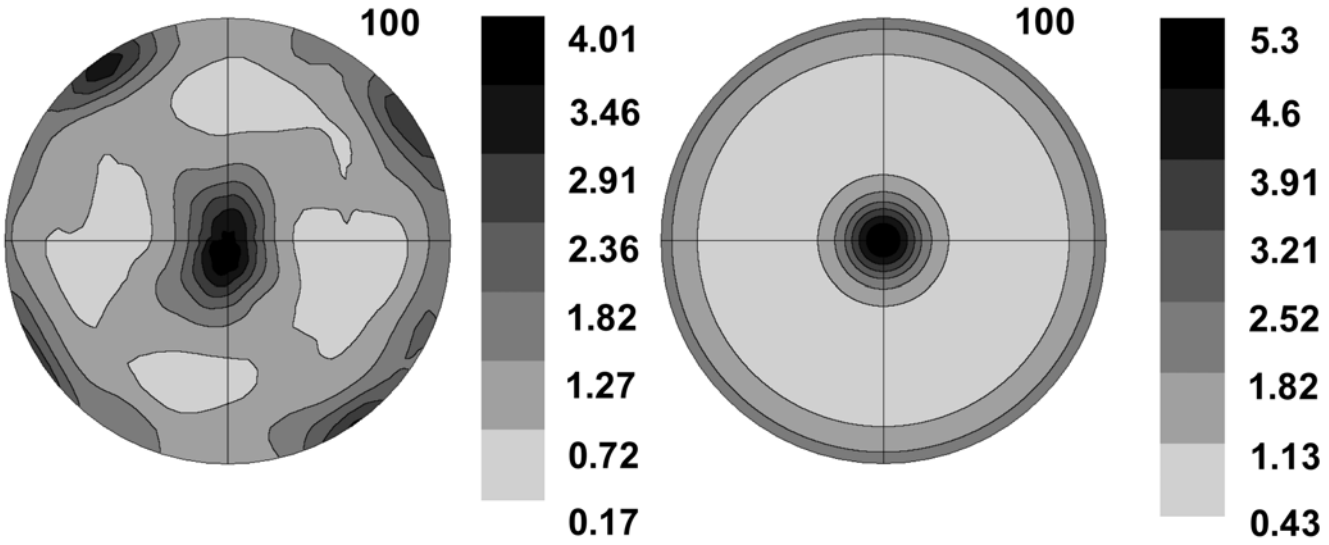
100
4.01
3.46
2.91
2.36
1.82
1.27
0.72
0.17
100
5.3
4.6
3.91
3.21
2.52
1.82
1.13
0.43

Figure 3a

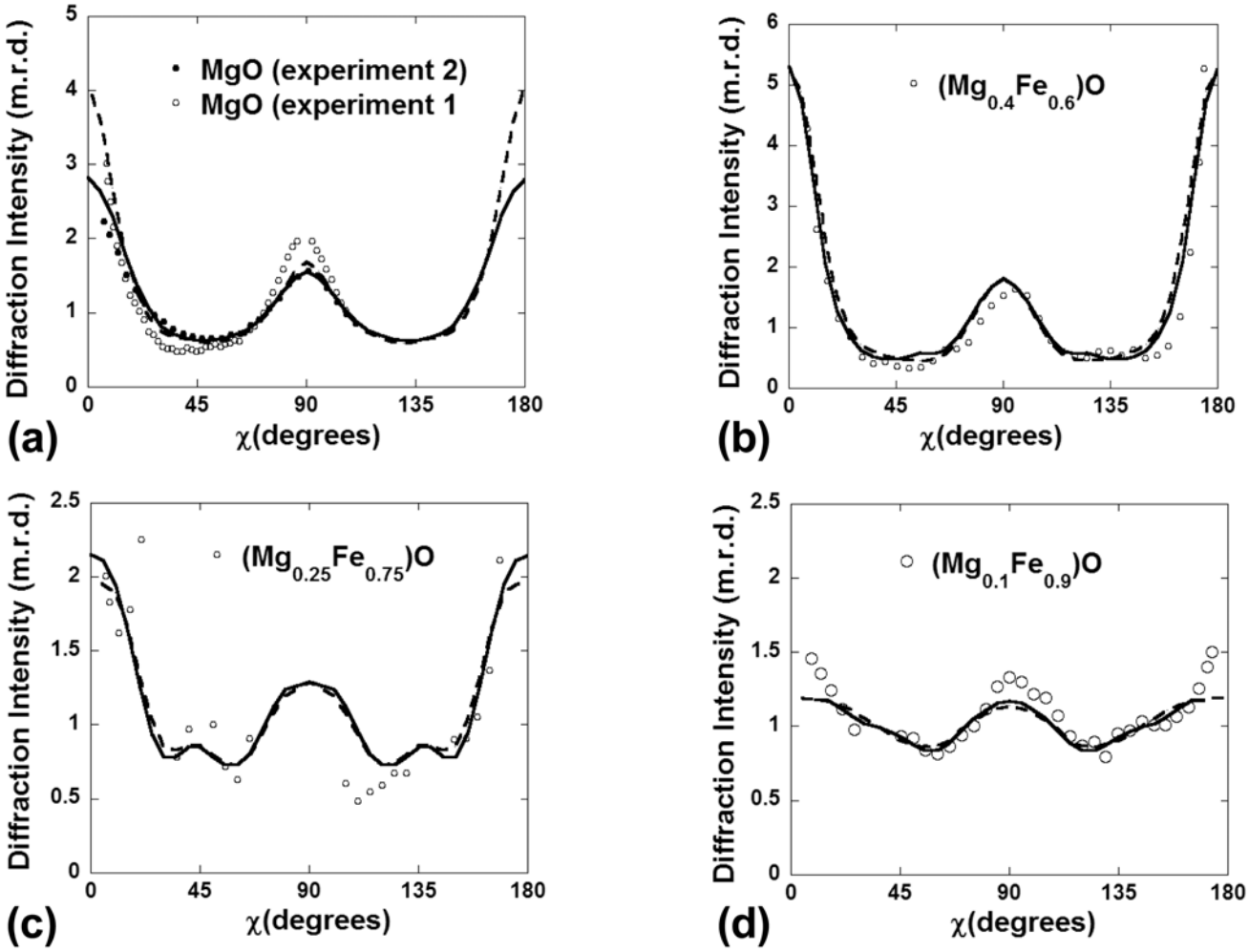
MgO (experiment 2)
MgO (experiment 1
Diffraction Intensity (m.r.d.)
χ(degrees)
(a)
(Mg0.4Fe0.6)O
(b)
(Mg0.25Fe0.75)O
(c)
(Mg0.1Fe0.9)O
(d)

Fgiure 4a-d

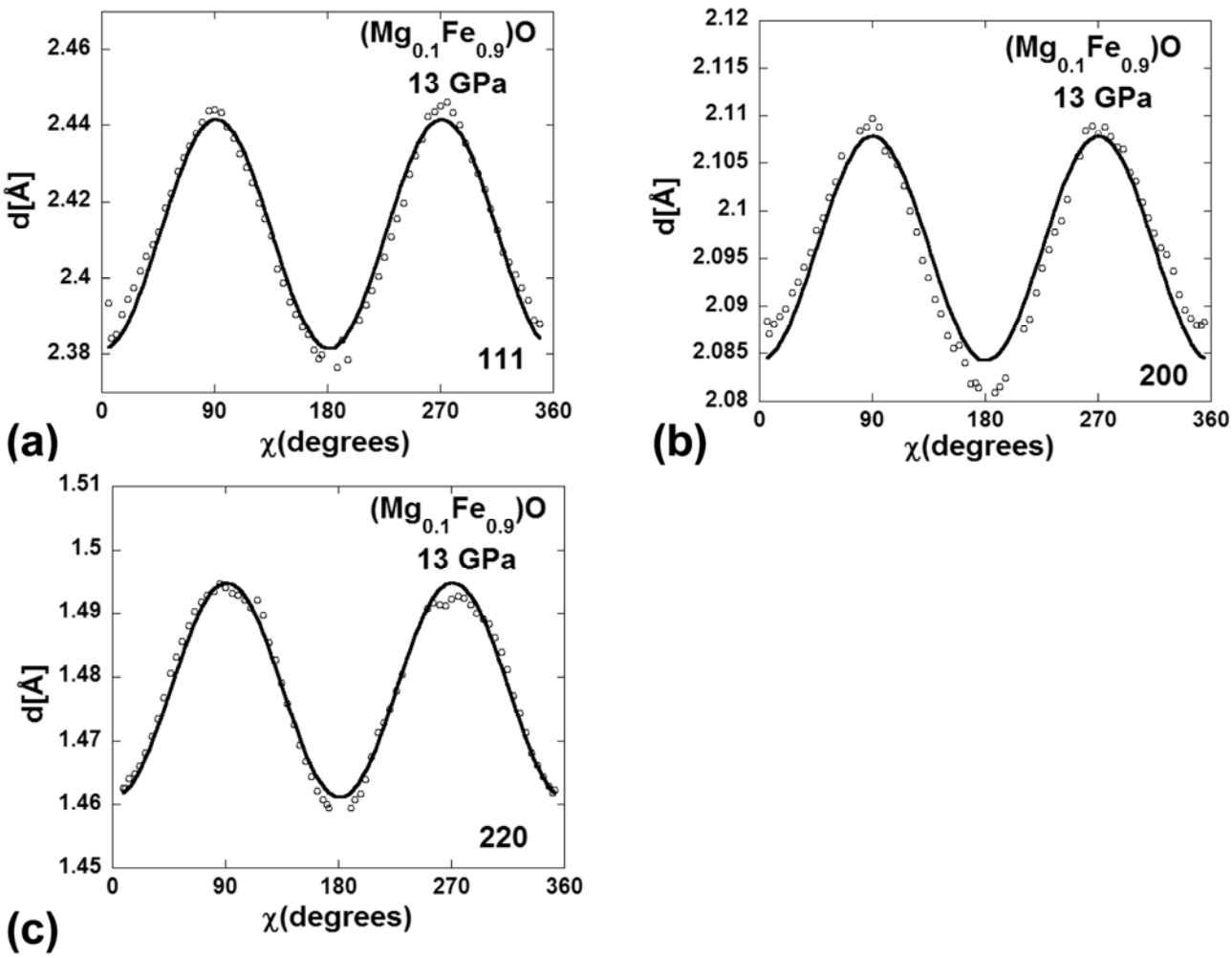
(Mg0.1Fe0.9)O
13 GPa
111
d[Å]
χ(degrees)
(a)
(Mg0.1Fe0.9)O
13 GPa
200
d[Å]
χ(degrees)
(b)
(Mg0.1Fe0.9)O
13 GPa
220
d[Å]
χ(degrees)
(c)

Figure 5a-c

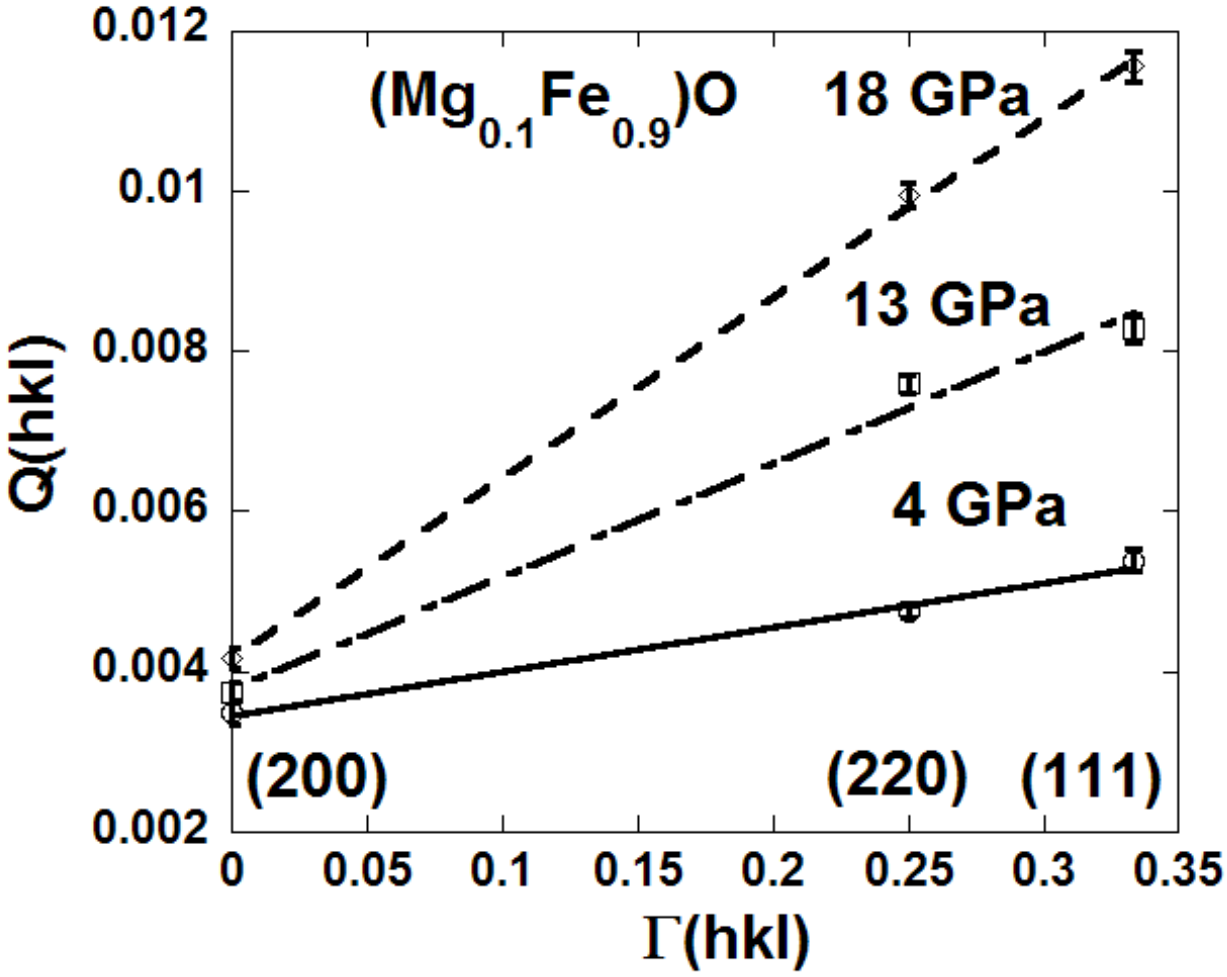
0.012
0.01
0.008
0.006
0.004
0.002
Q(hkl)
(Mg0.1Fe0.9)O
18 GPa
13 GPa
4 GPa
(200)
(220)
(111)
0
0.05
0.1
0.15
0.2
0.25
0.3
0.35
Γ(hkl)

Figure 6

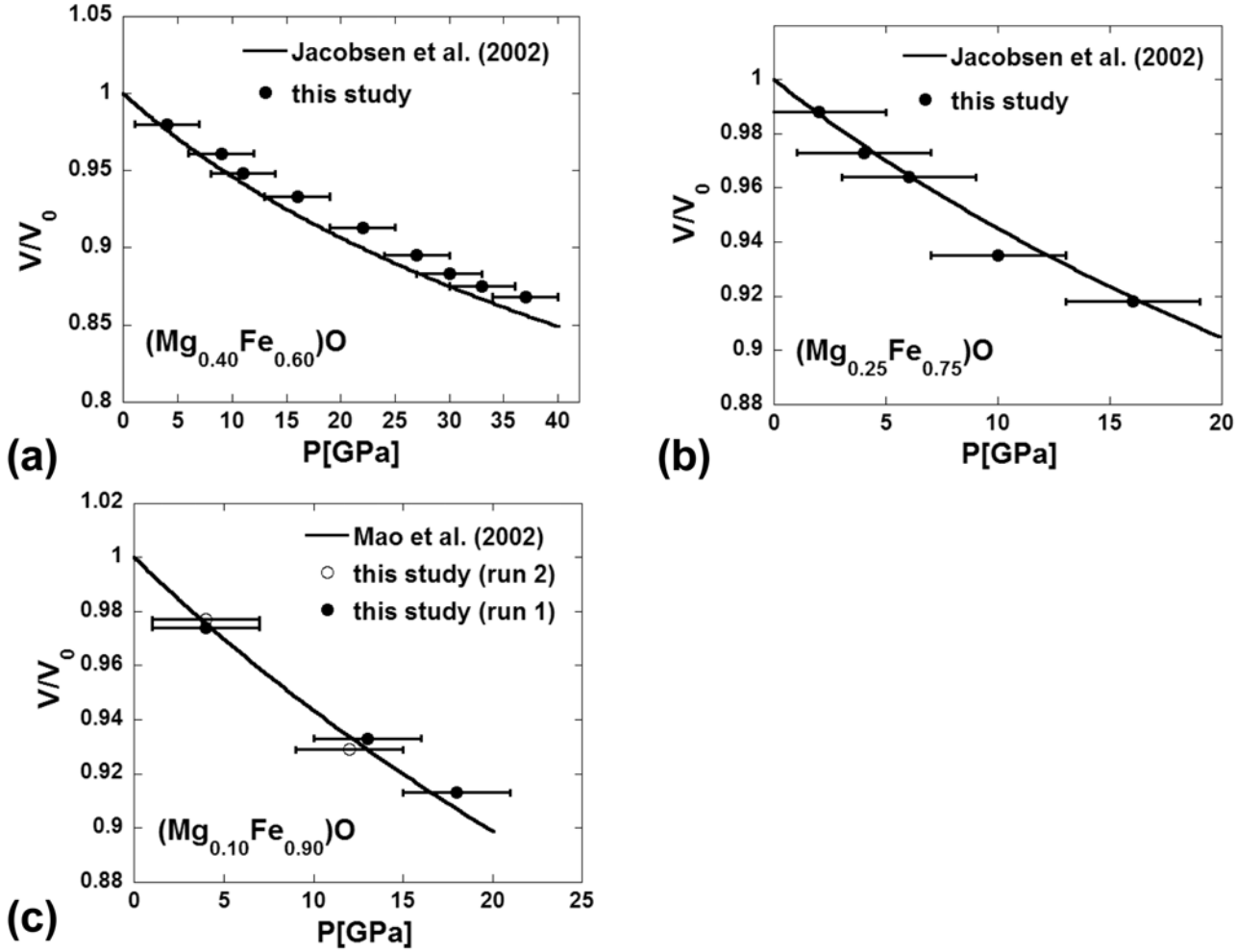
Jacobsen et al. (2002)
this study
(Mg0.40Fe0.60)O
V/V0
P[GPa]
(a)
Jacobsen et al. (2002)
this study
(Mg0.25Fe0.75)O
V/V0
P[GPa]
(b)
Mao et al. (2002)
this study (run 2)
this study (run 1)
(Mg0.10Fe0.90)O
V/V0
P[GPa]
(c)

Figure 7a-c

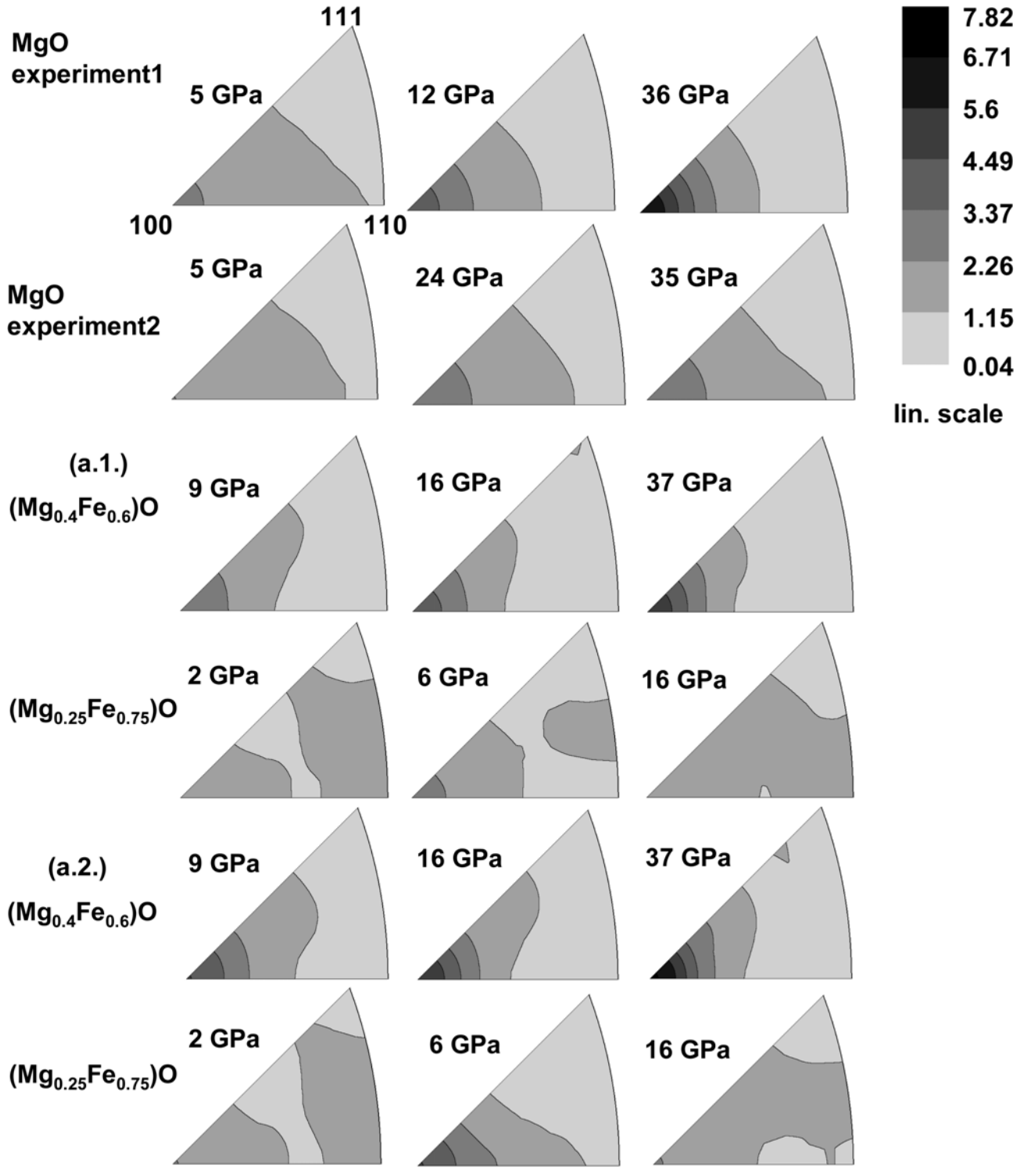
111
MgO
experiment1
5 GPa
12 GPa
36 GPa
100
110
5 GPa
24 GPa
35 GPa
MgO
experiment2
(a.1.)
(Mg0.4Fe0.6)O
9 GPa
16 GPa
37 GPa
(Mg0.25Fe0.75)O
2 GPa
6 GPa
16 GPa
(a.2.)
(Mg0.4Fe0.6)O
9 GPa
16 GPa
37 GPa
(Mg0.25Fe0.75)O
2 GPa
6 GPa
16 GPa
7.82
6.71
5.6
4.49
3.37
2.26
1.15
0.04
lin. scale

(a)

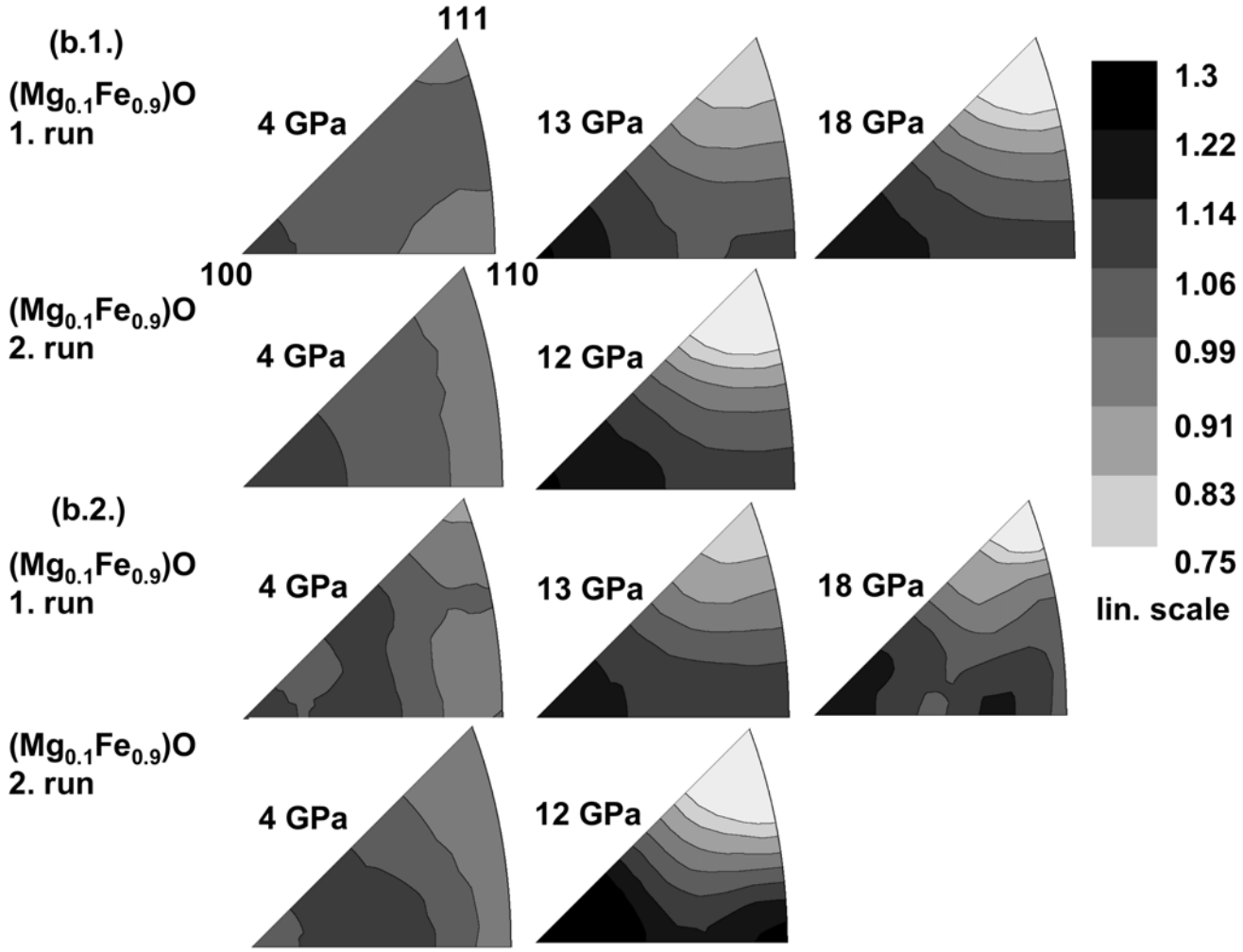
(b.1.)
(Mg0.1Fe0.9)O
1. run
111
4 GPa
13 GPa
18 GPa
100
110
(Mg0.1Fe0.9)O
2. run
4 GPa
12 GPa
(b.2.)
(Mg0.1Fe0.9)O
1. run
4 GPa
13 GPa
18 GPa
(Mg0.1Fe0.9)O
2. run
4 GPa
12 GPa
1.3
1.22
1.14
1.06
0.99
0.91
0.83
0.75
lin. scale

(b)
Figure 8a-b

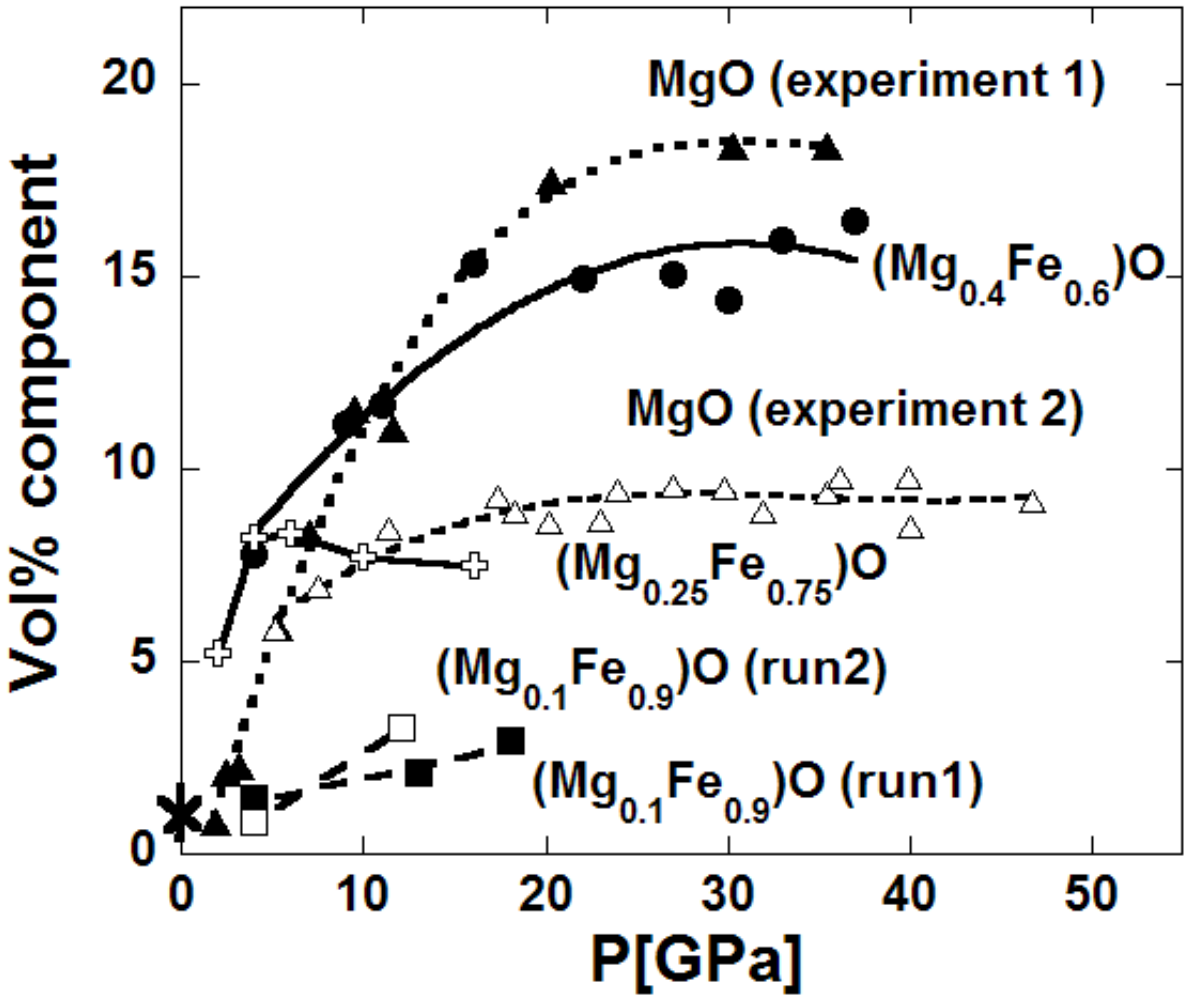
MgO (experiment 1)
(Mg0.4Fe0.6)O
MgO (experiment 2)
(Mg0.25Fe0.75)O
(Mg0.1Fe0.9)O (run2)
(Mg0.1Fe0.9)O (run1)
Vol% component
P[GPa]
0
5
10
15
20
0
10
20
30
40
50

Figure 9

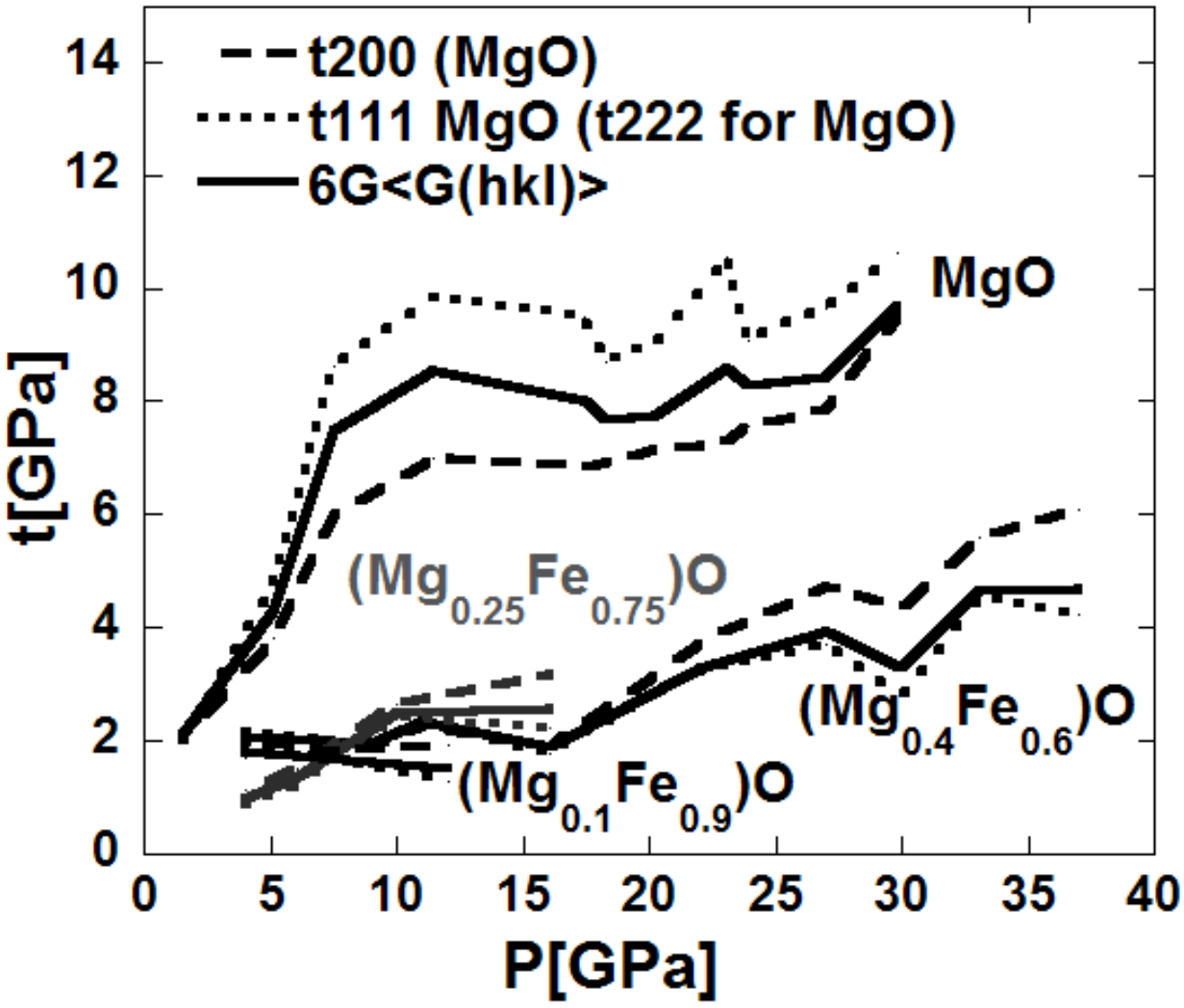
t200 (MgO)
t111 MgO (t222 for MgO)
6G<G(hkl)>
MgO
(Mg0.25Fe0.75)O
(Mg0.4Fe0.6)O
(Mg0.1Fe0.9)O
t[GPa]
P[GPa]
0
2
4
6
8
10
12
14
0
5
10
15
20
25
30
35
40

(a)

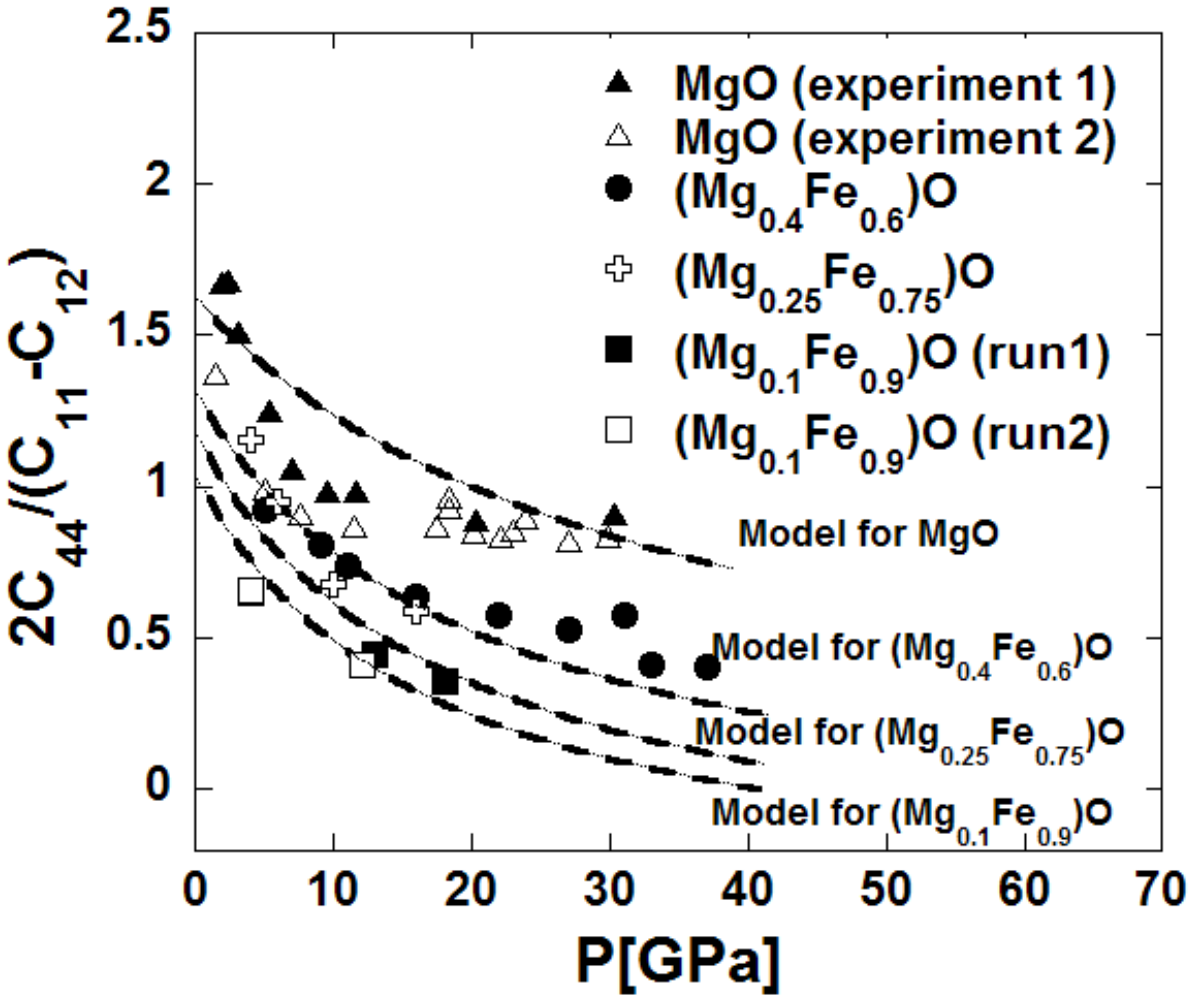

(b)
Figure 10a-b